HIROSHIMA UNIVERSITY

MASTER'S THESIS

Azimuthal correlation analysis of electron-muon pairs for heavy-flavor measurements in proton-proton collisions at $\sqrt{s} = 13.6$ TeV with ALICE

Author:
Shunsuke KURITA

Supervisor:
Prof. Kenta SHIGAKI
Examiner:
Prof. Atsushi NISHIZAWA
Prof. Zachary John LIPTAK

A thesis submitted in fulfillment of the requirements for the degree of Master of Science

in the

Quark Physics Laboratory
Graduate School of Advanced Science and Engineering

January 31, 2025

HIROSHIMA UNIVERSITY

Abstract

Physics Program
Graduate School of Advanced Science and Engineering

Master of Science

Azimuthal correlation analysis of electron-muon pairs for heavy-flavor measurements in proton-proton collisions at $\sqrt{s} = 13.6$ TeV with ALICE

by Shunsuke KURITA

At the CERN Large Hadron Collider (LHC), ultra-high-temperature states that existed in the early universe, known as quark-gluon plasma (QGP), are recreated through lead nucleus collisions for further study. In particular, heavy quarks (charm and beauty) are excellent probes because they are produced in the early stages of collisions, where predictions based on perturbative QCD calculations are applicable, and subsequently interact with the QGP. Therefore, it is important to measure the heavy quark production at the initial stage of a proton-proton collision, which serves as a baseline for accurate QGP research.

Since the main production mechanisms of heavy quarks exhibit different azimuthal dependencies, the azimuthal correlation of lepton pairs originating from heavy-quark decays allows us to disentangle their respective contributions. Specifically, there are leading-order (LO) processes where two quarks are emitted in opposite directions, as well as neaxt-leading-order (NLO) processes with distinct correlation patterns. At the LHC, due to the high beam energy, changes in the production process fractions are predicted because of effects such as gluon saturation and increased contributions from NLO processes. Thus, studying heavy-quark production in proton-proton collisions is essential. Previous studies have analyzed electron pairs and muon pairs, but these measurements face challenges in removing background contributions from resonance decays, thermal radiation, the Drell-Yan process, and jets.

In this study, we perform measurements using electron-muon pairs in the ALICE experiment. By using particle pairs with different electric charge lepton flavors, we can avoid background contributions from resonance decays, thermal radiation, and the Drell-Yan process. Additionally, due to the large pesudorapidity gap between ALICE's electron and muon detectors, contributions from near-side jet events can be suppressed.

This thesis presents an analysis of the azimuthal correlation of electron-muon pairs in proton-proton collisions at a center-of-mass energy of 13.6 TeV in the ALICE experiment. Using simulation data, a basic purity evaluation of single electrons and single muons was performed, and the azimuthal distribution of electron-muon pairs was obtained from real data. While the purity of single muons was nearly 100% and satisfactory, the purity of single electrons, when using standard selection cuts, was around 20%, indicating suboptimal performance. This result suggests that the selection conditions based on the energy loss in the main central detector need to be optimized for different transverse momentum ranges. Additionally, we performed heavy-quark selection using transverse momentum information and applied corrections for geometric acceptance effects using event mixing. The corrected azimuthal distribution showed a peak on the away side ($\Delta\varphi = \pi$), consistent with the expected contribution from the lowest-order production process.

Acknowledgements

First of all, I would like to express my gratitude to my supervisor, Professor Kenta Shigaki. He supported my research and gave me accurate advice. I would like to ask for his help when I proceed to the doctoral program. I would also like to thank Associate Professor Yorito Yamaguchi and Assistant Professor Satoshi Yano. Their advice at monthly meetings was helpful in determining the direction of my research. Also, Associate Professor Kensuke Homma and Assistant Professor Takahiro Miyoshi gave me comments on the important part of my interim report, which was my research motivation. I was also helped a lot by researchers at CERN. Dr. Fabio Filippo Colamaria and Dr. Fabrizio Grosa, conveners of the Heavy Flavor Physics Working Group, kindly explained many of my technical questions. At the Heavy Flavour Correlations and Leptons group meeting, Dr. Nicole Bastid and Dr. Jonghan Park consulted with me about the content and plan of the analysis. I would like to take this opportunity to express my gratitude. I am so grateful to Motomi Oya and Kento Kimura that I can't fit them all into this thesis. I have vivid memories of the fun times we spent together, talking about research, touring sake breweries, drinking in the Hiroshima city, and so on. Finally, I would like to thank my family and friends who supported me throughout my student life.

Contents

List of Figures

List of Tables

Chapter 1

Introduction

1.1 Quantum chromodynamics

Quantum chromodynamics (QCD) is one of the quantum field theories, and the SU(3) color gauge symmetry theory describes the interaction between quarks and gluons. In addition to flavor, quarks have three degrees of freedom: color likened to the three primary colors of light: R, G, and B. Anti-quarks correspond to anti-R, anti-G, and anti-B. Quarks interact with each other through gluons with eight color degrees of freedom and form hadrons in color singlet states, which are combinations of quarks whose color is white. The color degrees of freedom were introduced to address the non-existence of violation of the Pauli exclusion principle by color SU(3) decuplet particles, such as $\Delta^{++}(1232) = (u^{\uparrow}u^{\uparrow}u^{\uparrow})$.

QCD is the extension of QED. QED Lagrangian is derived by requiring U(1) gauge symmetry for the fermion field ψ_f and is described as

$$\mathcal{L}_{QED} = \sum_f \bar{\psi}_f (i\gamma^\mu \partial_\mu - m_f)\psi_f + e\sum_f Q_f \bar{\psi}_f \gamma^\mu \psi_f A_\mu - \frac{1}{4} F_{\mu\nu}F^{\mu\nu} \tag{1.1}$$

where the first term is the free particle term, second is the interaction term between charged particle f and electromagnetic fields, and third is the electromagnetic field term.

Similarly, QCD Lagrangian is derived by requiring SU(3) gauge symmetry for the quark field $\psi_{q,a}$ and is described as

$$\mathcal{L}_{QCD} = \sum_q \bar{\psi}_{q,a} (i\gamma^\mu \partial_\mu - m_q)\psi_{q,a} + g_s \sum_q Q_f \bar{\psi}_{q,a} \gamma^\mu T^A_{ab} \psi_{q,b} G^A_\mu - \frac{1}{4} G^A_{\mu\nu} G^{A\mu\nu} \tag{1.2}$$

where g_s is the coupling constant, the first term is the free quark term, second is the interaction term between quark q and gluon fields G^A_μ, and third is the gluon field term. The subscripts q and a, b denote the flavor and color of quarks each other, and superscript A denotes the color carried by gluons.

1.1.1 Asymptotic freedom

One of the key characteristics that distinguishes QCD from QED is the self-interaction of gluons as gauge fields. The coupling constant of QED (QCD) depends on the square of momentum transfer Q^2. This phenomenon occurs when field theory includes vacuum polarization effects from charge (color charge) through higher-order

loop corrections. In the case of QED, the effective coupling constant is [1]:

$$\alpha_{\text{eff}}(Q^2) = \frac{\alpha}{1 - \frac{\alpha}{3\pi} \ln\left(\frac{Q^2}{m_e^2}\right)} \tag{1.3}$$

On the other hands, the effective coupling constant of QCD is expressed as

$$\alpha_s(Q^2) \equiv \alpha_{\text{eff}}(Q^2) = \frac{\alpha(\mu^2)}{1 + \alpha(\mu^2)\frac{\beta_0}{4\pi} \ln\left(\frac{Q^2}{\mu^2}\right)} \tag{1.4}$$

$$\beta_0 = 11 - \frac{2}{3} n_f \tag{1.5}$$

where μ is the renormalization scale, and n_f is the number of flavors.

The coupling constant depends on the renormalization scale, which can be chosen arbitrarily. So, a new constant Λ_{QCD} that does not depend on Q^2 and μ^2 is introduced.

$$\frac{1}{\alpha(Q^2)} + B(Q^2) = \frac{1}{\alpha(\mu^2)} + B(\mu^2) \equiv -\frac{\beta_0}{4\pi} \ln\left(\Lambda_{QCD}^2\right) \tag{1.6}$$

The leading log approximation (LLA) of α_s using Λ_{QCD} is given as follows:

$$\alpha_s(Q^2) = \frac{4\pi}{\beta_0 \ln\left(Q^2/\Lambda_{QCD}^2\right)} = \frac{12\pi}{(33 - 2n_f) \ln\left(Q^2/\Lambda_{QCD}^2\right)} \tag{1.7}$$

Figure 1.1 shows the Q^2 dependence of the QCD coupling constant. Black line is a theoretical calculation result including quantum effects up to 5 loops. The theoretical and measured values are consistent.

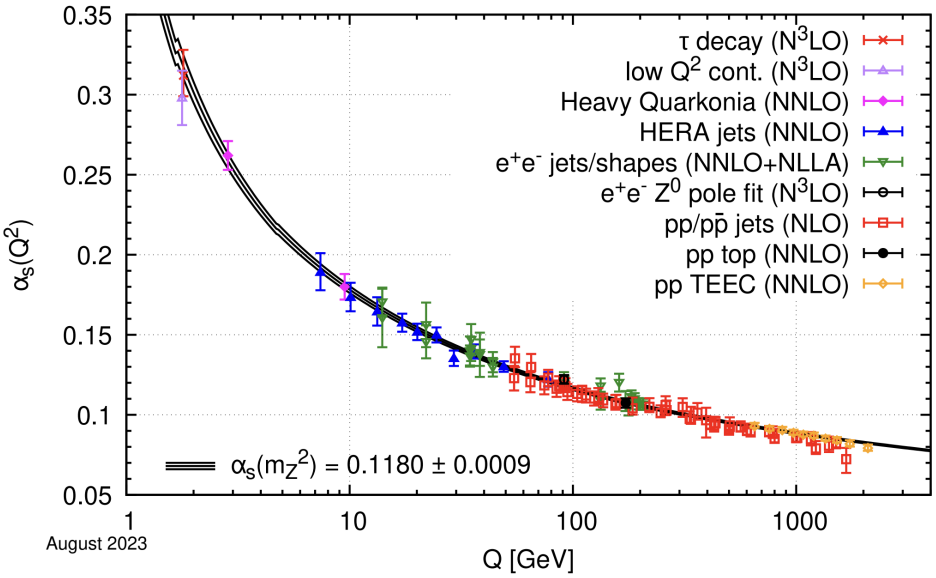

FIGURE 1.1: Q dependence of the QCD coupling constant [2]

Regarding the QED coupling constant, the coupling constant becomes smaller as the distance increases. Conversely, the QCD coupling constant becomes smaller at short distances, that is, quarks and gluons influence free particles in the reaction with large momentum transfer. This property is called asymptotic freedom.

1.1.2 Perturbative QCD

It is difficult to solve the QCD Lagrangian strictly, so the approximation using perturbative calculations whose perturbation terms is interaction terms is used. Perturbation calculations of physical quantities are generally expressed in the form of powers of α_s.

$$P = c_1\alpha_s + c_2\alpha_s^2 + \cdots \tag{1.8}$$

This is valid in the high energy region where $\alpha_s \ll 1$, *i.e.* $\Lambda_{QCD} \ll Q^2$. In contrast, it diverge at low energy region, particularly for $\Lambda_{QCD} \sim Q^2$.

1.2 Heavy-flavor physics

Heavy flavors (charm and beauty) are quarks with large masses. In high-energy hadronic collisions, they are mainly generated in initial hard parton scattering processes due to the large mass.

$$\tau_{HF} \lesssim 1/m_{HF} \approx 0.05\text{-}1.00\ \mathrm{fm}/c \tag{1.9}$$

They then evolve into parton showers and become hadrons, collectively known as fragmentation. Their large mass makes perturbative QCD calculations valid even at low p_T ($m_{HF} \gg \Lambda_{QCD}$). For example, the calculation of heavy-flavor production cross section is based on the factorization theorem, which separates into perturbative and non-perturbative parts (see Figure 1.2).

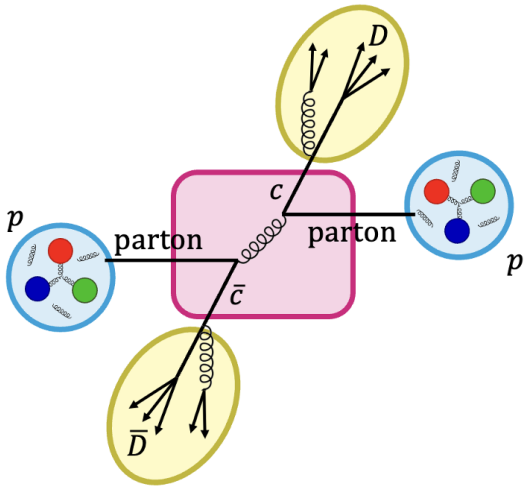

$$\sigma_{\mathrm{hh}\to\mathrm{Hh}} = \mathrm{PDF}(x_a, Q^2)\mathrm{PDF}(x_b, Q^2) \otimes \sigma_{ab\to q\bar{q}} \otimes D_{q\to\mathrm{h}}(z_q, Q^2)$$

FIGURE 1.2: Charm quark production in proton-proton (pp) collisions. Partonic cross section (Magenta) is a perturbative part. Parton distribution functions (Cyan) and fragmentation function (Yellow) are non-perturbative parts.

1.2.1 Heavy flavors as probes

Heavy flavors are a sensitive tool for studying the physics of strong interactions. Heavy-flavor measurements in pp collisions are most suitable to test QCD calculations and serve as baseline for studies in heavy-ion collisions.

The Figure 1.3 and left side of Figure 1.4 show the $b\bar{b}$ and $c\bar{c}$ production cross section in pp collisions. It can be seen that the theoretical predictions and measurements agree well within the uncertainty range.

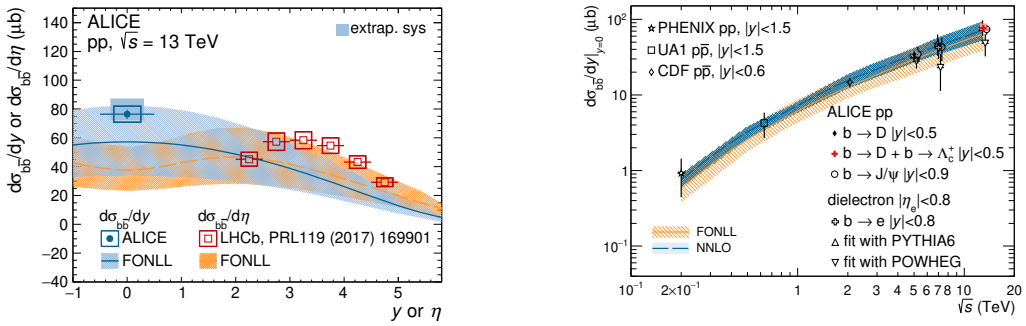

FIGURE 1.3: Left: $b\bar{b}$ production cross section per unit of pseudo-rapidity in pp collisions at midrapidity as a function of the rapidity. Right: $b\bar{b}$ production cross section per unit of rapidity in pp collisions at midrapidity as a function of the center-of-mass energy [3].

The right side of Figure 1.4 shows the charm quark fragmentation fraction in pp collisions. The studies regarding baryon-to-meson and meson-to-meson ratio lead to the understanding the parton distribution function and fragmentation function.

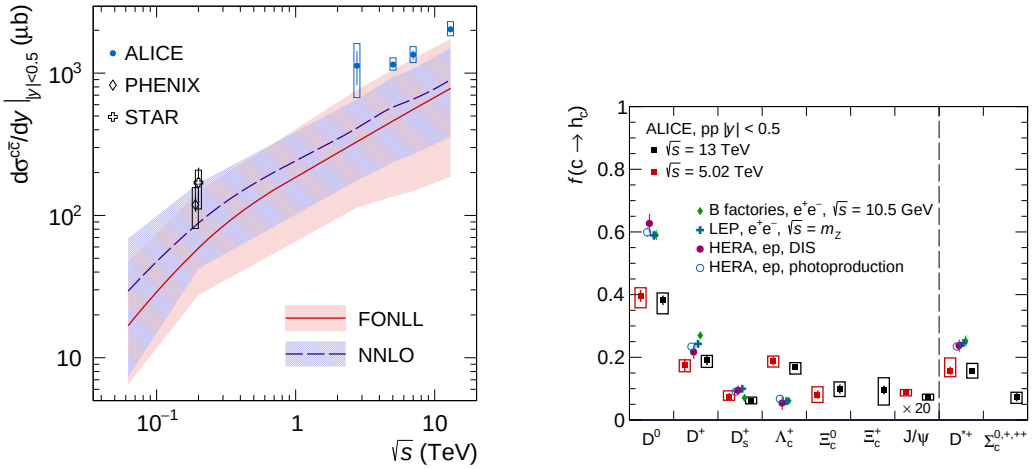

FIGURE 1.4: Left: $c\bar{c}$ production cross section per unit of rapidity in pp collisions at midrapidity as a function of the center-of-mass energy. Right: charm quark fragmentation fractions in pp collisions at midrapidity compared with electron-positron and electron-proton collisions [4].

The fragmentation functions are generally believed to be universal across collision systems, but the baryon-to-meson ratios of high multiplicity pp and p-A collisions have been shown to differ from those of ee and ep collisions (see Figure 1.5

and left side of Figure1.6).

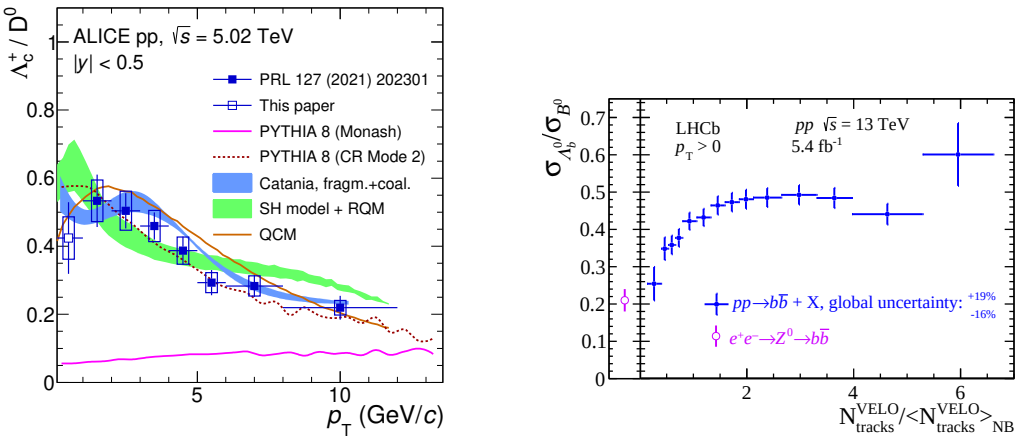

FIGURE 1.5: Left: Λ_c^+/D^0 ratio as a function of pT in pp collisions [5]. Right: Λ_b^0/B^0 ratio as a function of the total track multiplicity measured in the VELO detectors (blue), measured in e^+e^- collisions at LEP (purple) [6].

We introduced the differences between ee, ep collisions and pp, p-A collisions above, but the differences between pp collisions and p-A collisions have also been measured. The observed differences between pp collisions and p+A or d+A collisions, where the presence of nuclei in the initial state may affect the final production of observed matter, are called Cold Nuclear Matter (CNM) effects. The right side of Figure 1.6 is a schematic diagram showing the Bjorken-x dependence of several phenomena thought to be CNM effects.

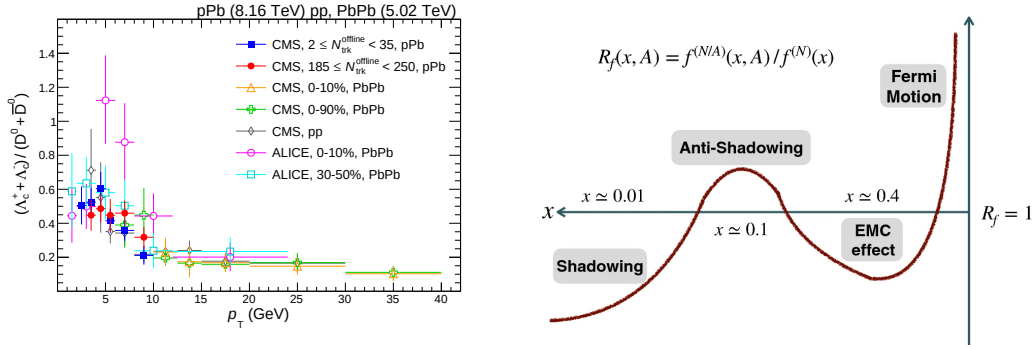

FIGURE 1.6: Left: Λ_c^+/D^0 ratio as a function of pT in p-A and A-A collisions [7]. Right: Schematic representation of different types of nuclear modifications [8].

If these effects exist they can affect the production of heavy flavors and therefore must be taken into account for the correct interpretation of heavy ion collisions. Figure 1.7 shows some example of CNM effects studies.

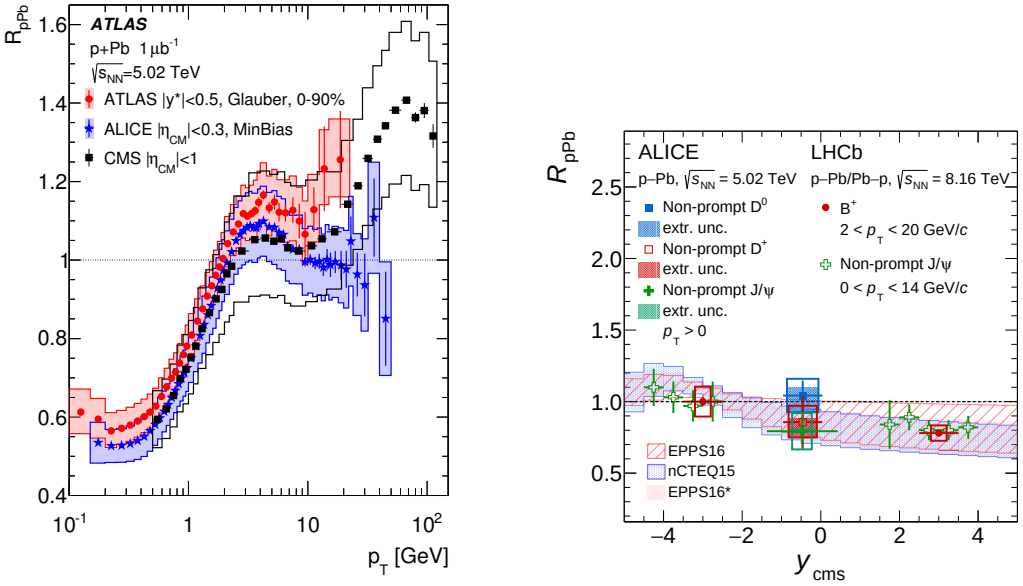

FIGURE 1.7: Left: The nuclear modification factor of charged hadrons in p-Pb collisions [9]. Right: pT integrated nuclear modification factor of D-mesons and J/ψ vs. rapidity [10].

Heavy flavors are one of the great probes to study Quark-Gluon Plasma (QGP) since they experience the medium evolution in heavy ion collisions entirely due to their early production. In addition, they carry color charge and have larger masses than the components of the QGP, allowing them to interact with the QGP medium while remaining distinguishable from it for tracking purposes. To study the properties of a medium, we need to focus on the collective motion of particles or media that can be distinguished from the medium. Figure 1.9 shows a part of example of studying the QGP.

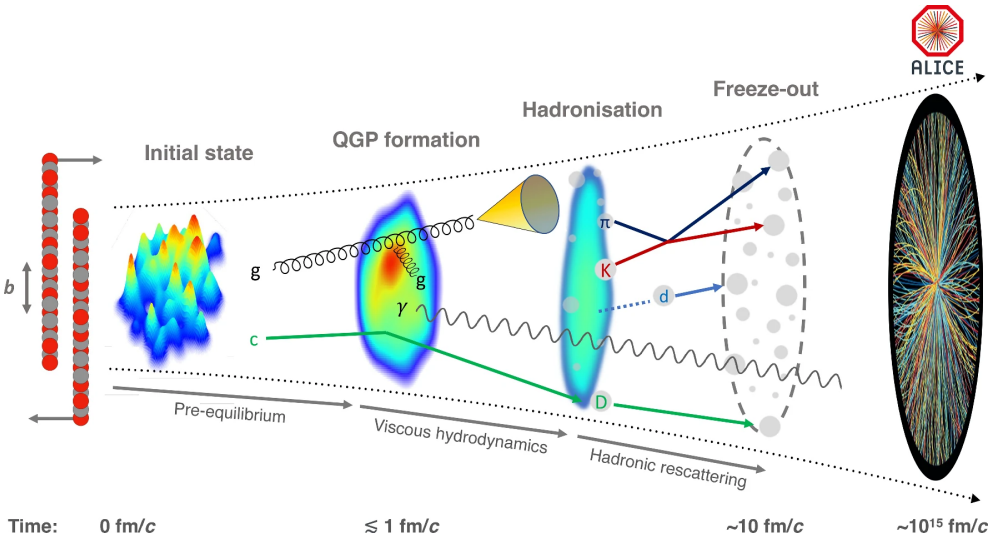

FIGURE 1.8: The evolution of a heavy-ion collision at LHC energies [11]

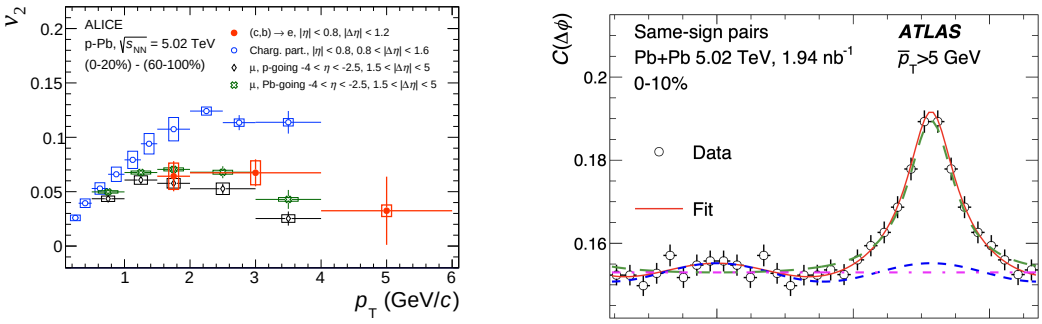

FIGURE 1.9: Tools of the medium evolution, two-particle correlations. Left: Elliptic flow [12]. Right: Azimuthal angular correlations [13].

1.2.2 azimuthal angular correlations in pp collisions

One measurement particularly sensitive to the production mechanism of heavy quarks is the azimuthal correlation distribution of lepton pairs generated from heavy-flavor hadron decays. More specifically, heavy-flavor quark pairs can be produced by leading-order (LO) processes, Flavor Creation (Figure 1.10), characterized by back-to-back azimuthal correlation of the two quarks, or next-to-leading-order (NLO) processes, Flavor Excitation (Figure 1.11) and Gluon Splitting (Figure 1.12), with a different correlation pattern [14]. The relative contribution of LO and NLO processes can be investigated from the azimuthal correlation distribution of the final-state heavy-flavor particles, and it is possible to set constraints to theoretical models describing this observable by comparing their predictions to the measurements.

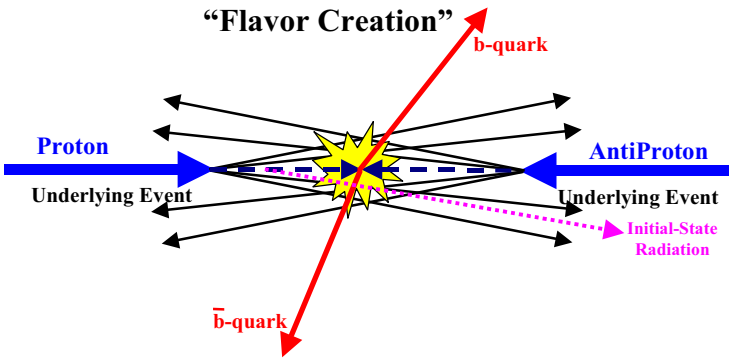

FIGURE 1.10: Flavor Creation. The gluons inside the protons fuse during the collision, producing $Q\bar{Q}$.Since the momentum of the original protons is $(0, 0, p_z)$ and $(0, 0, p'_z)$, momentum is conserved on the x-y plane, and the pair-generated $Q\bar{Q}$ is emitted back-to-back, *i.e.*, in the opposite direction. Therefore, there is a peak at $\Delta\varphi = \pi$.

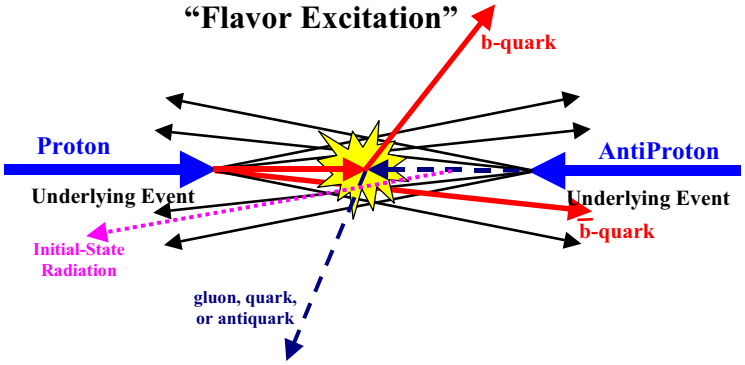

FIGURE 1.11: Flavor Excitation. Heavy quarks that exist as "sea quarks" inside the proton are "excited" by interactions with partons in the initial state and appear in the final state.

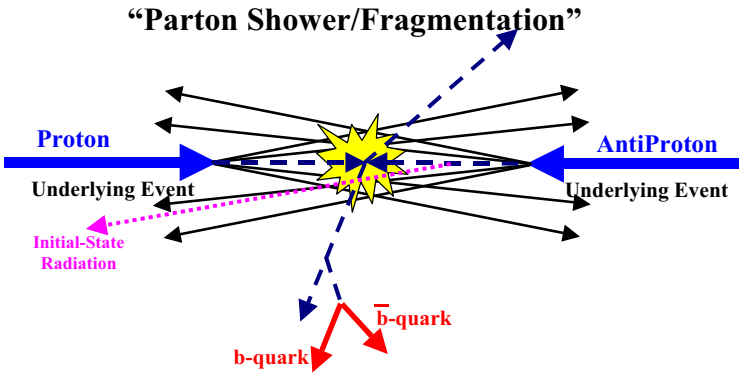

FIGURE 1.12: Gluon Splitting. When the high-energy gluons that emerge from the collision have enough energy to produce heavy quarks, they can "split" into heavy quarks. Since the gluons split in the direction they are flying, it is thought that $\Delta\varphi$ becomes narrower.

Of course, the measurement works as the baseline of the QGP study. For instance, regarding the right side of Figure 1.9, by comparing with the results of pp collisions where QGP does not occur, we can see how much the heavy quarks deviate from their original orientation after diffusion. If there was diffusion, the peak width of the back-to-back heavy-flavor muon correlation signal would be broader than that resulting from pp collisions.

1.3 Electron-muon correlations

The background events in the azimuthal correlation analysis are the contributions of jets, which are a small concentration of energetic particles, and decays from resonance states. Both have high energies and are therefore difficult to distinguish from the heavy quark signal. We perform the analysis using the electron-muon pair with ALICE detectors this time. Figure 1.13 is a signal example of the electron-muon pair.

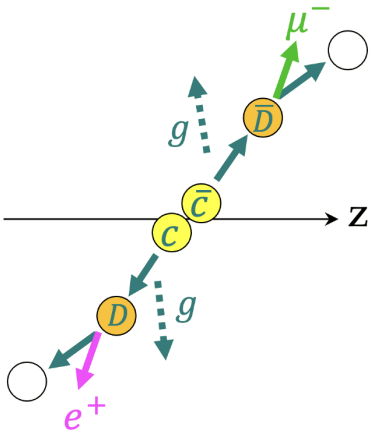

FIGURE 1.13: Signal example of the electron-muon pair

By using electron-muon pairs, the background events mentioned above can be suppressed. Regarding the jet, in the ALICE experiment, there is a large gap in the rapidity between the detector that identifies the electrons and the spectrometer that identifies the muons. This allows the contribution of the jet that appears on the nears-side $(\Delta\eta, \Delta\varphi) = (0, 0)$, to be suppressed. Details of the detector will be discussed in Chapter 2.

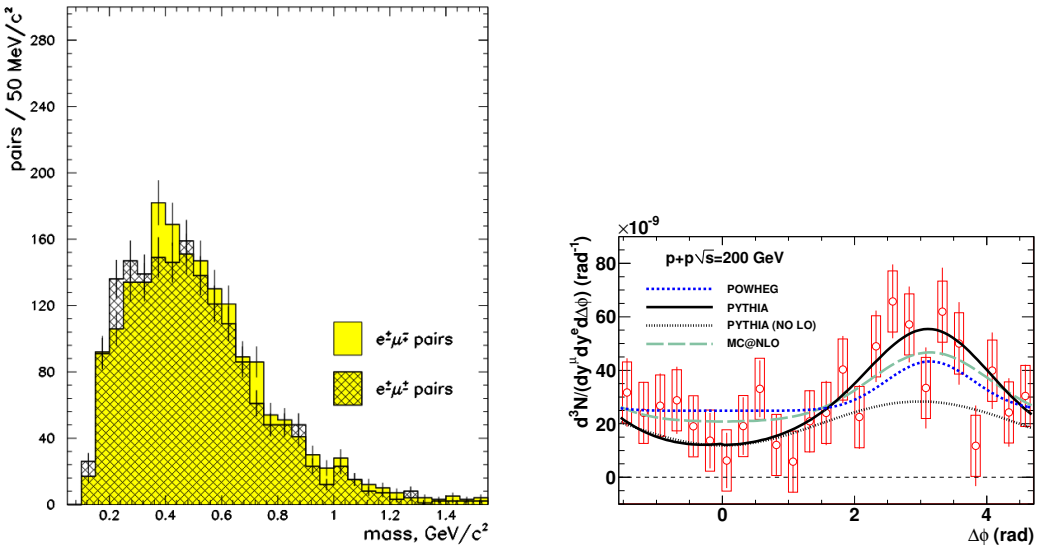

FIGURE 1.14: Measurements of electron-muon correlations. Left: Mass distribution with HELIOS [15]. Right: Azimuthal angular correlation with PHENIX [16].

This measurement also allows us to perform clean measurements that suppress electromagnetic processes conserving the flavor lepton number, as Drell-Yan process and resonance decays. Figure 1.14 shows previous research using electron-muon pairs. Many analyses use electron-electron pairs or muon-muon pairs, so the triggers used to acquire data are often suitable for these. Therefore, even if data on both electrons and muons is acquired, it is not necessarily possible to analyze electron-muon correlations. In addition, there is little previous research on suppressing the contribution of jets, which is one of the benefits of using electron-muon correlation,

because it may not be possible to obtain the benefit depending on the detector arrangement.

1.4 Purpose of my thesis

In this study, we aim to analyze the azimuthal correlation from heavy flavors using electron-muon pairs in the ALICE experiment. The LHC-ALICE experiment Run 3, which began in 2022, has been upgraded specifically for heavy flavor measurements. In addition, the introduction of a new continuous readout has made it possible to perform electron-muon correlation analysis. In this thesis, we perform an analysis of the azimuthal correlation of electron-muon pairs in pp collisions, which serves as a baseline for other collision systems.

Chapter 2

Experimental Setup

2.1 Large Hadron Collider (LHC)

The Large Hadron Collider (LHC) is the world's most powerful circular particle accelerator. Its ring is 27 km long and built at a mean depth of 100 m. It accelerates the hadrons close to the speed of light and collides them at each collision point (Point 1: ATLAS, Point 2: ALICE, Point 5: CMS, Point 8: LHCb). The energy of the center mass as of Run 3 is 13.6 TeV for proton-proton collisions and 5.36 TeV for Pb-Pb collisions. O-O collisions are also planned for 2025 runs. The CERN accelerator complex is shown in Figure 2.1.

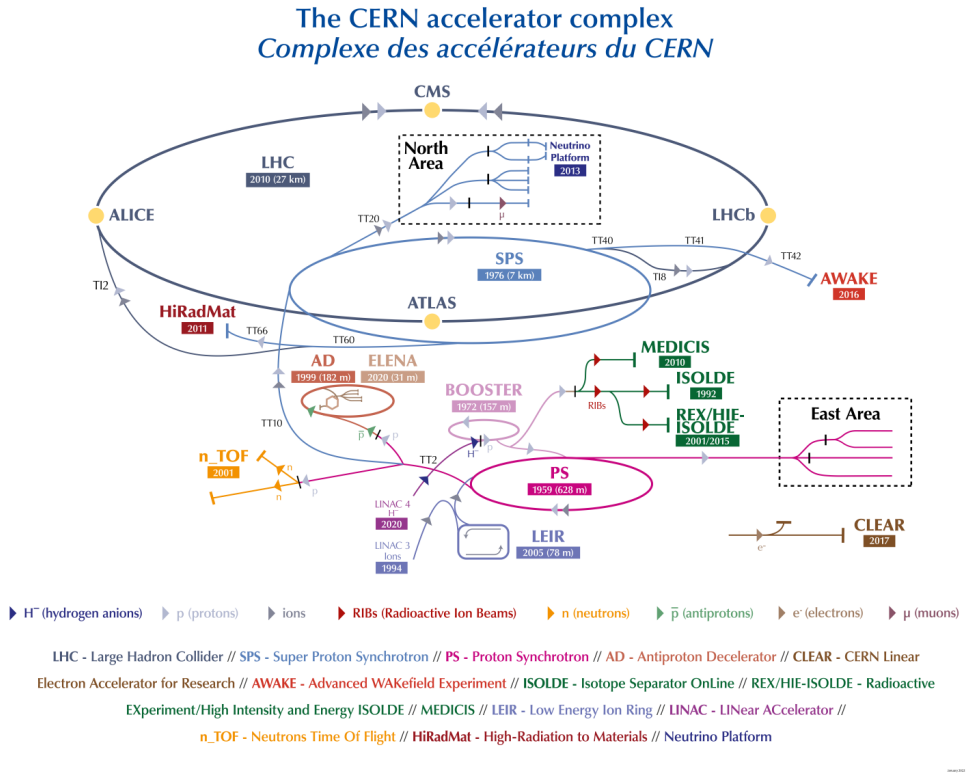

FIGURE 2.1: The CERN accelerator complex [17]

Protons are gotten by stripping a electrons from a hydrogen atoms. Protons are injected to the PS BOOSTER (PSB) with 50 MeV, and the PSB accelerates protons to 1.4 GeV. Then, the beam is traveled to Proton Synchrotron (PS) and accelerated to 25 GeV. Next, the beam is sent to Super Proton Synchrotron (SPS) and accelerated to 450 GeV. Finally, the beam reaches to the LHC and is accelerated to 6.8 GeV while rotating clockwise (or counterclockwise). The bunch spacing is 25 ns.

Figure 2.2 shows the sectional view [18] and picture of the LHC superconducting dipole magnets. The magnets are cooled to 1.9 K by liquid helium circuits to keep the superconducting states. Inside there are pipes for both clockwise and counterclockwise beams. The pipes maintain the ultra-vacuum states as empty as outer space to avoid colliding between residual gases in the tubes and the beam.

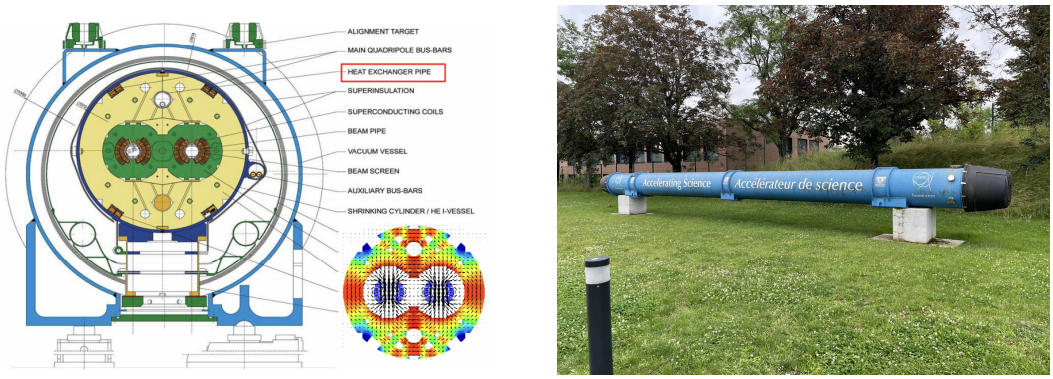

FIGURE 2.2: Sectional view [18] and picture of the LHC superconducting dipole magnets

2.2 ALICE apparatus

A Large Ion Collider Experiment (ALICE) is the only experiment specific to heavy ion experiments in the LHC. The apparatus (Figure 2.3) consists of central barrel detectors covering a rapidity region $|\eta| < 0.9$ and forward detectors covering the region $-2.5 < \eta < -4$.

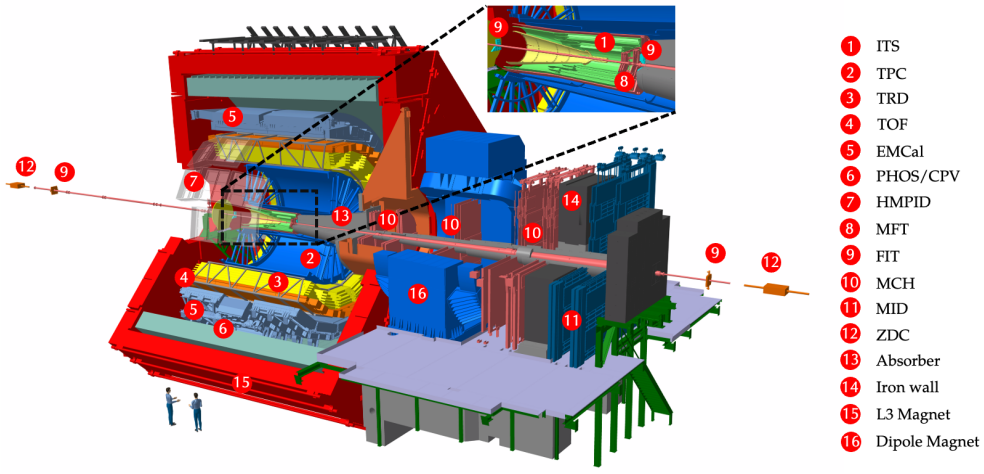

FIGURE 2.3: The global view of the ALICE apparatus

In Run 3, data was acquired at a readout rate of 500 kHz, which is 500 times faster than in Run 2. To achieve this, several detectors including readout system were upgraded during Long Shutdown 2 (LS2).

2.2.1 Central barrel detectors

All central barrel detectors are housed inside a large solenoid magnet called L3 magnet. The maximum magnetic field is 0.5 T parallel to the beam axis.

Inner Tracking System

The Inner Tracking System (ITS) is a tracker covering $|\eta| < 1.22$ and all azimuthal angle range. The main functions of this detector are to determine the primary vertex, reconstruct the secondary vertex, and identify low-momentum particles. It also helps to improve the momentum and angular resolution of particles reconstructed by the Time Projection Chamber (TPC). It consists of three inner barrel layers of silicon pixel detector (SPD) and four outer barrel layers (two silicon drift detectors (SDD) and two silicon strip detectors (SSD)). The silicon chip used is CMOS monolithic active pixel sensors (MAPS) that integrates electronic circuits and silicon sensors, which make it possible to achieve high resolution (spatial resolution of 5 micrometers) with a low material budget.

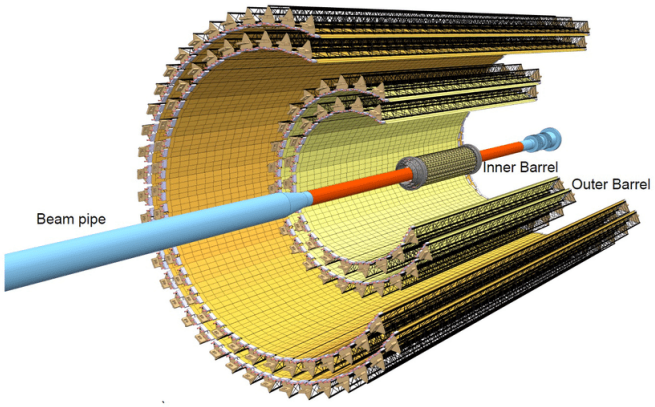

FIGURE 2.4: Layout of the Inner Tracking System [19].

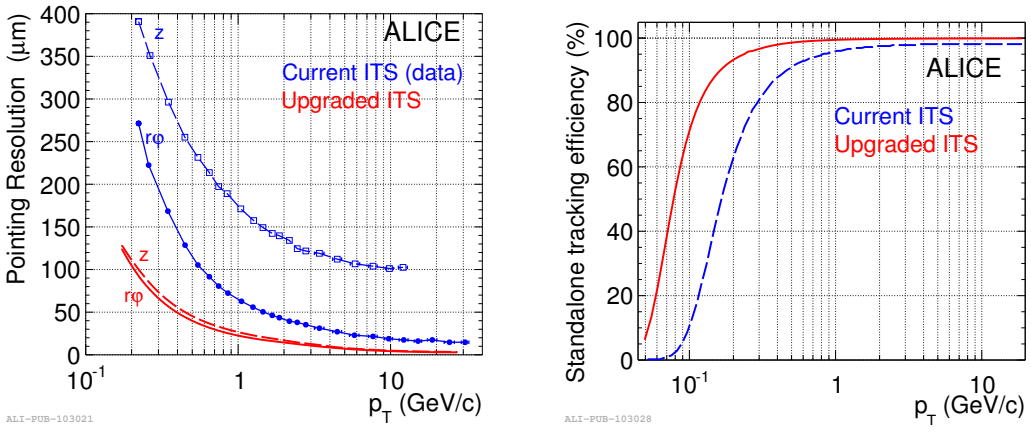

FIGURE 2.5: ITS resolution (left) and efficiency(right) [20].

Time Projection Chamber

The Time Projection Chamber (TPC) is the main gas detector responsible for tracking and identification of particles in ALICE. It is cylindrical with an outer diameter and length of 5 m, and covers all azimuthal angles and $|\eta| < 0.9$. By applying a voltage of 100 kV to the central HV electrode installed in the center, a drift field of 400 V/cm is generated in the direction of the end caps on both sides. Charged particle passes through the TPC while being bent by the magnetic field of the solenoid magnet. The mixed gas inside the TPC is ionized along the trajectory of the charged particles, and the drift field induces the electrons to be guided to the readout section as a signal. The maximum drift time is 92 ns. If the induced signal, *i.e.*, charge, exceeds a threshold and meets all the required quality criteria, it is called a cluster. The ionization energy loss, 3D trajectory, and momenta of charged particles are decided by combining the cluster information and the information of another detector such as ITS, TOF, etc.

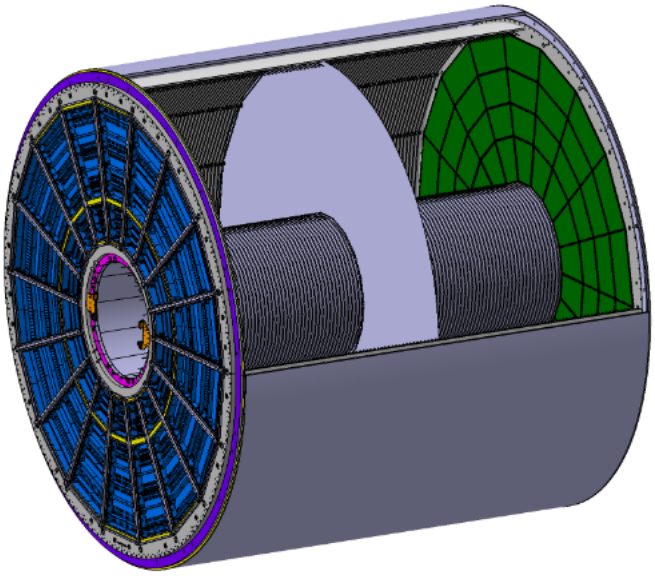

FIGURE 2.6: Layout of the Time Projection Chamber [21].

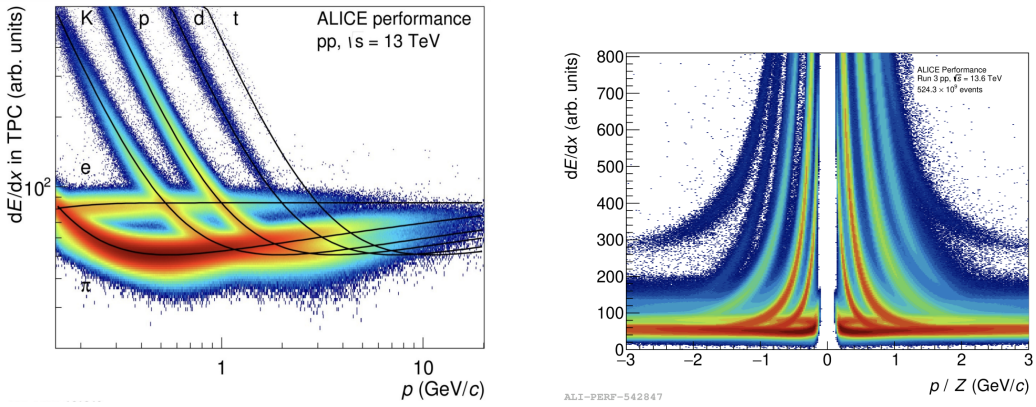

FIGURE 2.7: TPC dE/dx vs Momentum performance plots with Run 2 (left) and Run 3 (right) [22].

The Multi-Wire Proportional Chambers (MWPC) were used for readout until Run 2. The readout rate was limited to approximately 3 kHz due to the need to mitigate distortions in the drift electric field caused by positive ions generated during the multiplication process. During the LS2 hardware upgrade, a 4-layer GEM foil was installed. This design allows amplification to be performed in stages, blocking about 99% of the positive ion backflow while still achieving the required amplification. As a result, the readout rate was significantly improved, enabling continuous readout.

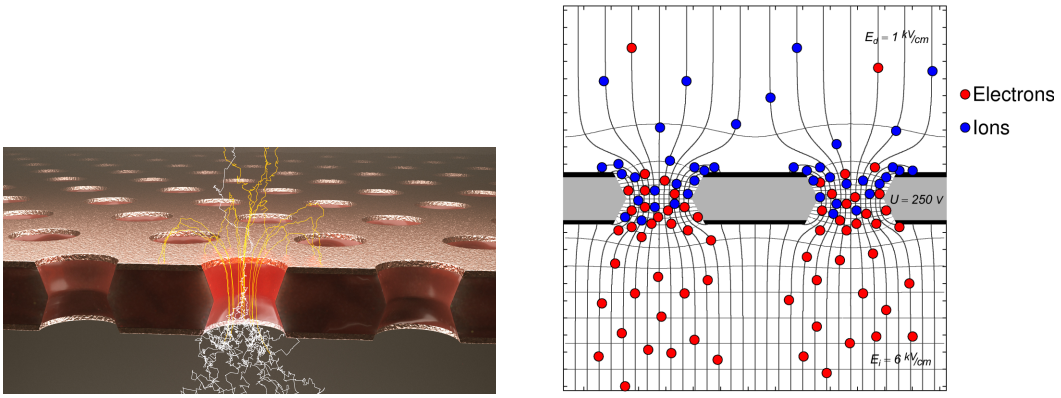

FIGURE 2.8: Left: arfield simulation of an electron avalanche in a GEM foil [23]. Right: Sketch of the working principle of a GEM [24].

Time Of Flight

The Time Of Flight (TOF) plays a role in charged particle identification in intermediate momentum. The coverage is all azimuthal angles and $|\eta| < 0.9$. Particle identification is performed by calculating β using the particle flight time from the collision vertex to the TOF. The time resolution is about 50 ps.

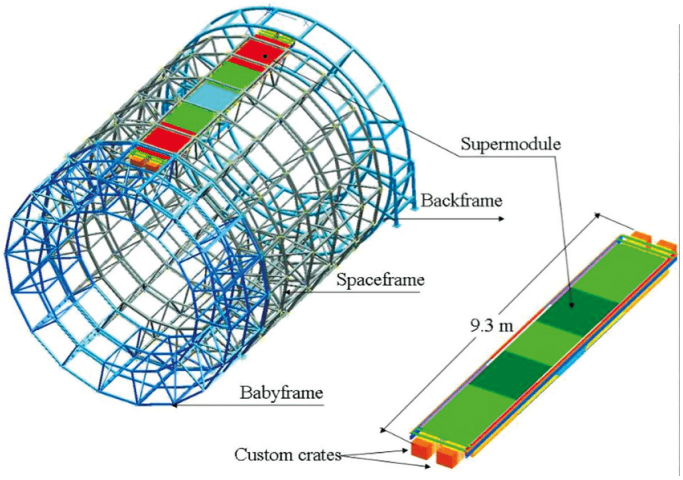

FIGURE 2.9: Layout of the Time Of Flight [25].

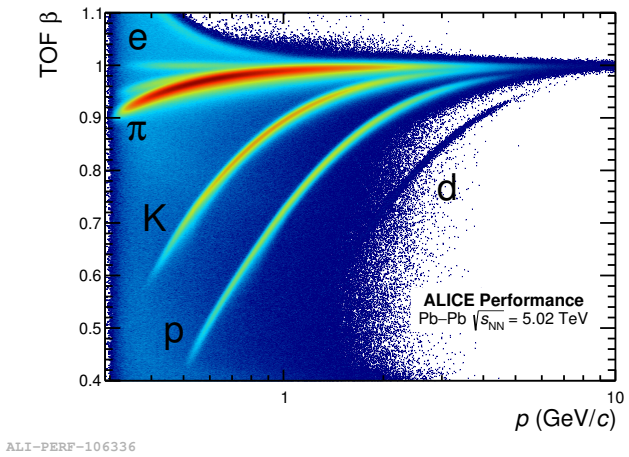

FIGURE 2.10: TOF Beta vs Momentum performance plot in Pb-Pb at 5.02 TeV [26].

Electro Magnetic Calorimeter

The Electro Magnetic Calorimeter (EMCal) is the shashlik-type lead-scintillator sampling calorimeter, and enhances the measurement capabilities of high energetic electrons, photons, jets and so on. The coverage is $|\eta| < 0.7$ and $80^\circ < \varphi < 187^\circ$. The EMCal has additional part which locate about π opposite in azimuthal angle from the main part. The aim of that is to measure the di-jet emitting back-to-back , so it is called Di-jet Calorimeter (DCal) when we want to distingwish to the main part of EMCal. The coverage of the DCal is $0.22 < |\eta| < 0.7$, $260^\circ < \varphi < 320^\circ$ and $|\eta| < 0.7$, $320^\circ < \varphi < 327^\circ$. The energy of photon or electron are measured via the number of photons produced by the electromagnetic shower.

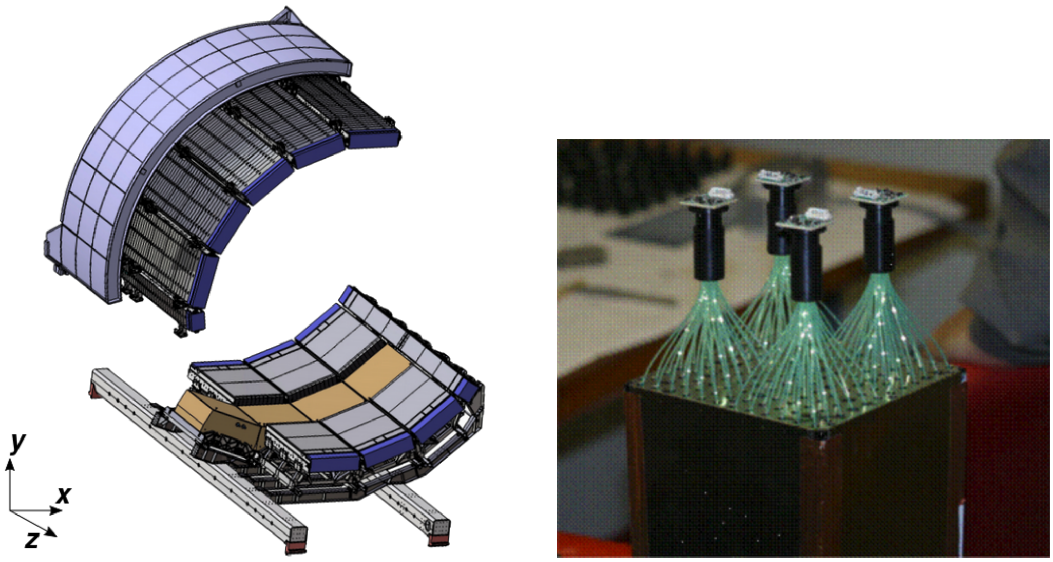

FIGURE 2.11: Left: Schematic view of the EMCal [27]. Right: Picture of a single prototype module with four towers [28]. The structure in which the optical fiber pierces the lead and the scintillator is the shashlik-type.

Electrons are identified using the ratio of the energy E measured by the EMCal to the momentum $\boldsymbol{p}$ obtained by the TPC. In high energy experiments, the following equation holds true because $|\boldsymbol{p}|^2 \gg m_e^2$:

$$E = \sqrt{|\boldsymbol{p}|^2 + m_e^2} \sim p \ ,\therefore E/p \sim 1 \tag{2.1}$$

So we can extract electrons by applying the E/p and the $n\sigma$ cuts.

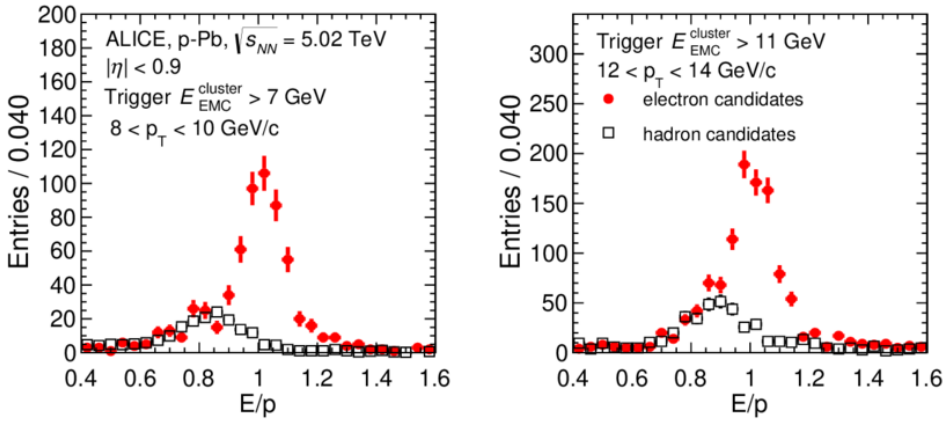

FIGURE 2.12: Electron identification using the EMCal [29].

2.2.2 Forward detectors

The ALICE coordinate system is a right-handed Cartesian coordinate system whose origin is interaction point 2. The z-axis is the counterclockwise direction around the LHC, and the x-axis points to the center of the LHC. The side with the muon arm at z=-1 is called the C-side, and the side at z=+1 is called the A-side.

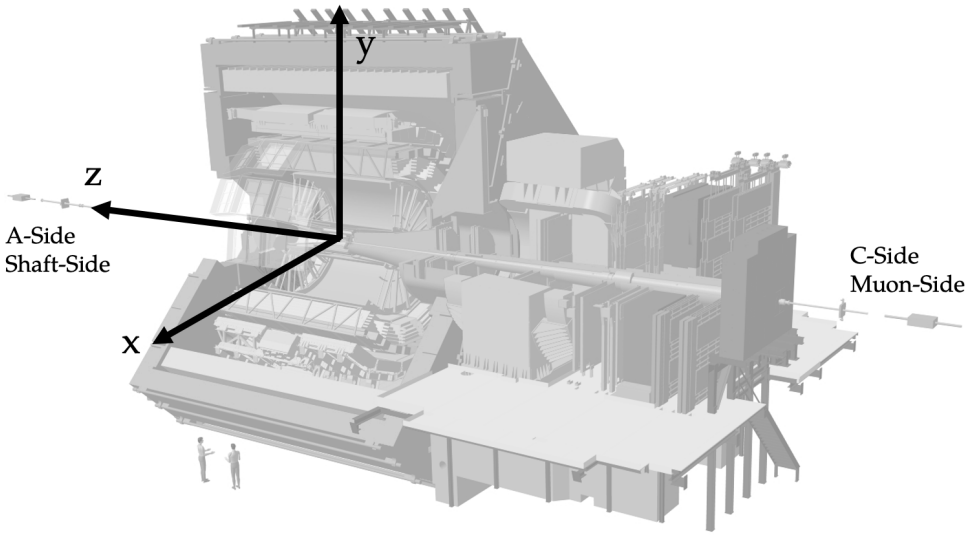

FIGURE 2.13: The coordinate of the ALICE apparatus

Fast Interaction Trigger

The Fast Interaction Trigger (FIT) is a new detector composed of Cherenkov arrays and plastic scintillators. It comprises three subdetectors: FT0, FV0, and FDD. The main role of the FIT is luminosity monitoring and providing plenty of trigger menus based on minimum-bias and centrality-based triggers. FIT serves data on the precise collision time for TOF particle identification. It also gives us the global collision parameters such as centrality and event plane.

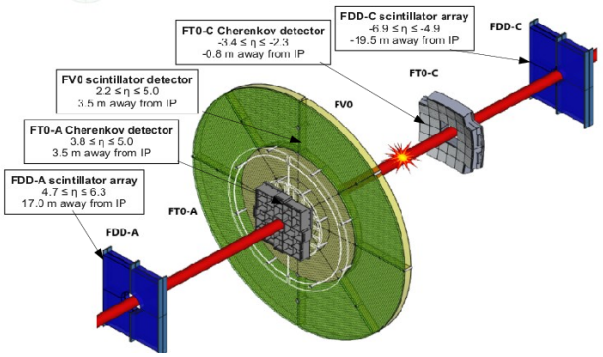

FIGURE 2.14: Layout of the Fast Interaction Trigger [30].

The following bullet points are brief summary of the sub detectors' components; characteristic; main roles:

- FT0: Two Cherenkov arrays on both sides; Low latency, Time resolution of 26 ps for minimum-bias pp collisions; Minimum-bias and centrality trigger generation, Collision time and vertex position calculations.
- FV0: Five scintillator rings; Low latency, Large coverage, Time resolution of about 250 ps; Background monitoring, Multiplicity trigger.
- FDD: Two scintillator arrays, two layers each; very forward rapidity; Tagging diffractive events, Background monitoring.

Cable-induced latency limit the use of the FDD as an online trigger detector [31].

Muon Forward Tracker

The Muon Forward Tracker (MFT) consists of the silicon pixel sensors covering all azimuthal angles and $-3.6 < \eta < -2.45$. The MFT uses the same silicon chips as the new ITS. This detector is added improving vertexing capabilities to muon tracking at forward rapidity. We match muons before and after the absorber. We match muons before and after the absorber using MFT (before) and MCH (after). Using the MFT information, we can reduce the influence of multiple scattering in the absorber and get the precise azimuthal angle and rapidity.

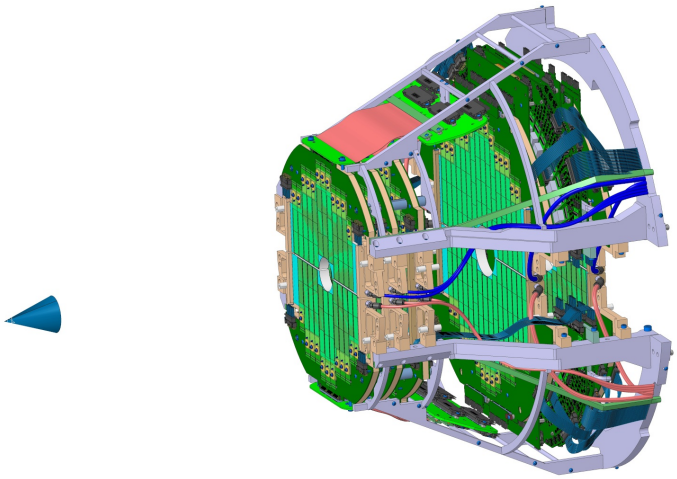

FIGURE 2.15: Layout of the Muon Forward Tracker [32].

Muon Spectrometer

Muon detectors are located in the forward rapidity region. There are two absorbers and two kinds of detectors. Regarding absorbers, There is a front absorber for suppressing particles except muons coming from the interaction vertex and an iron wall to vetoing particles except muons coming from multiple scattering with the front absorber.

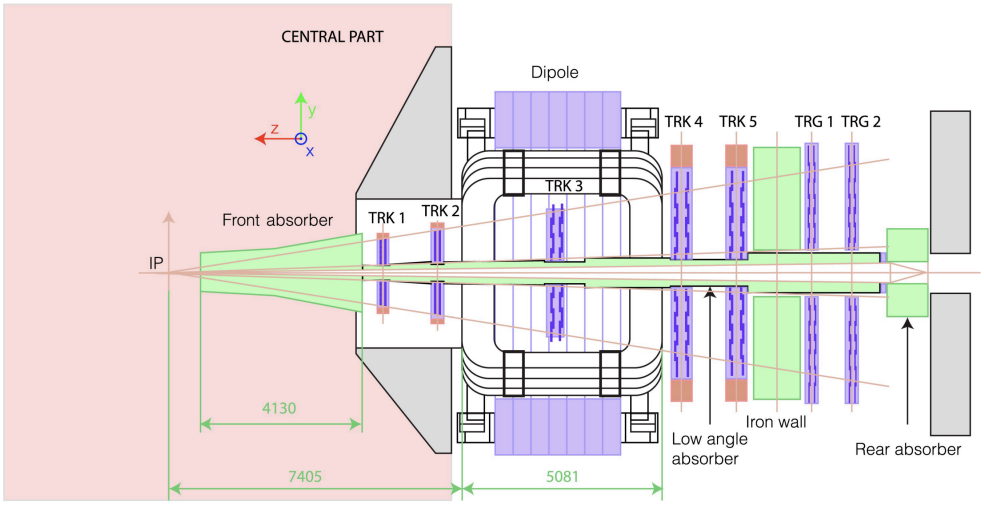

FIGURE 2.16: Layout of the Muon Spectrometer, MCH and MID [33].

Muon CHamber

Muon CHamber (MCH) is the muon tracking system. The MCH requires a spatial resolution better than 100 mm and achieves the resolution by reducing material budgets ($< 3\%$ X_0 per chamber [34]) to minimize the muon scattering. X_0 means a radiation length.

Muon IDentifer

Muon IDentifer (MID) is the detector located at the very end of the muon spectrometer. It serves as the muon trigger system. The MID has a < 25 ns time resolution since it must be possible to distinguish 25 ns bunch crossings.

2.2.3 Online-Offline Computing System O^2

The measurements in the ALICE Run 3 focuses on precise measurements and studies of the QGP via rare probes including heavy-flavor particles. In conventional trigger measurements, it was difficult to access rare event probes with small S/B ratios. In ALICE, data taking with continuous readout has been performed since Run 3. This makes it possible to avoid trigger dead-time and enables measurements with high statistics that do not miss rare events. On the other hand, the data rate of heavy ion collision events is 3.4 TB/s. From a readout and storage perspective, we need as fast and massive compression of the data flow as possible. The new introduced computing system achieving such huge amount of data handling is O^2.

Detectors send data as a continuous stream, so the problem is how to synchronize the data between detectors and how to split the data. For triggered measurements, data coming from the same trigger can be grouped together. O2 uses dedicated time markers to split these data flows into manageable pieces called time frames (TFs), and synchronizes, aggregates and buffers the data relative to the LHC clock.

A two-step online data reduction is performed. Data from each detector is collected by First Level Processors (FLPs). The collected data is then reduced background hit by identifying TPC clusters (charge deposits along the particle trajectory through the TPC gas). This reduces the data volume by a factor of 2.5. The data is then merged, split into sub-time frames (STFs), and buffered until it is sent to Event Processing Nodes (EPNs), where online tracking and reconstruction are performed. The raw data is replaced with these corrected data and saved in storage.

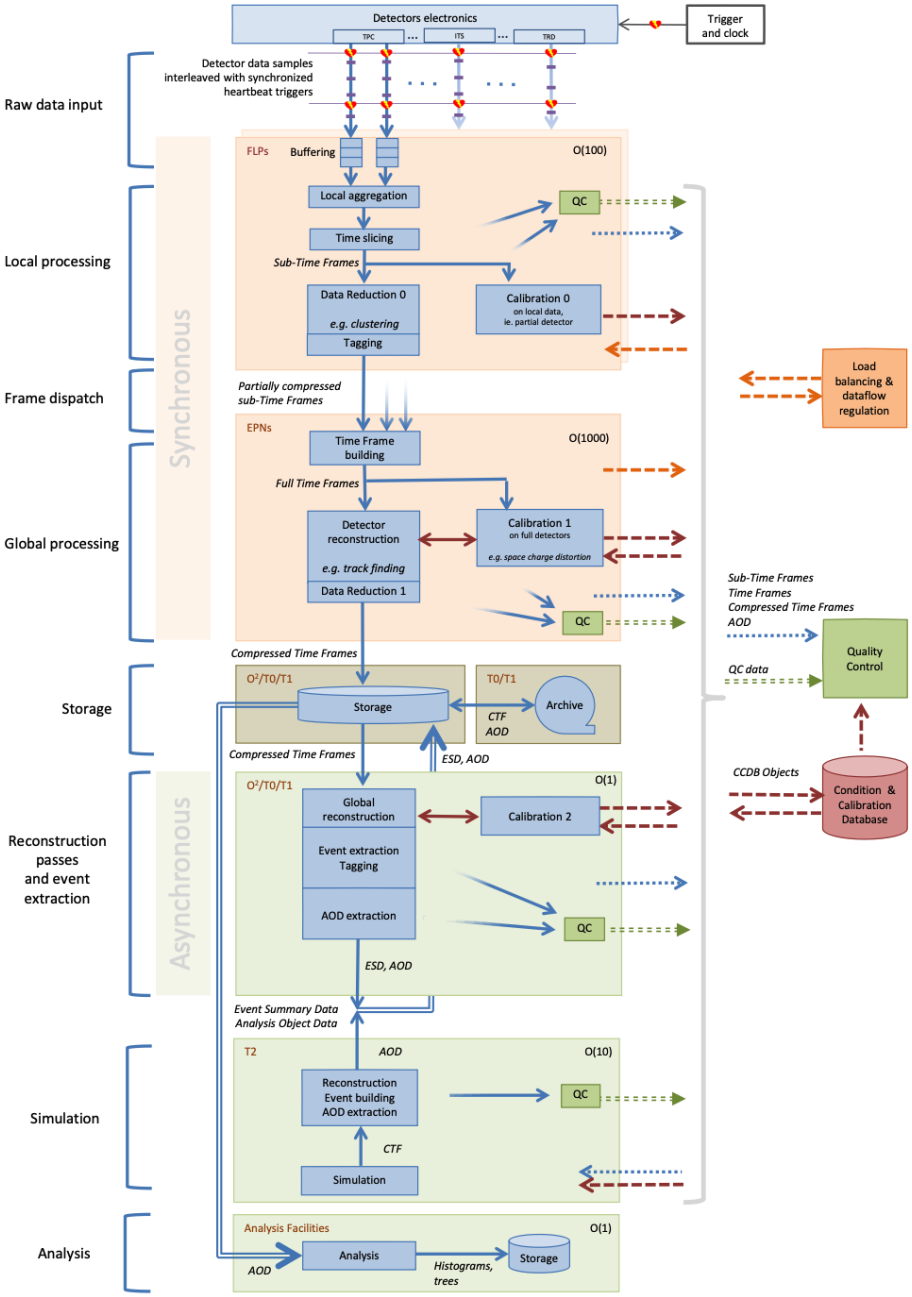

FIGURE 2.17: Data flow and processing pipeline of the O^2 system [35].

Chapter 3

Analysis

The real data used in this study are part of the minimum-bias data for 13.6 TeV proton-proton collisions taken by the ALICE experiment in 2022. These data are taken by the continuous readout, *i.e.*, trigger-less measurements, but some bias occurs during data processing. That's why it's called minimum-bias data rather than no-bias data. In terms of Monte Carlo data, event generation in 13.6 TeV proton-proton collisions, detector response of ALICE using Geant4, Geant3, and/or FLUKA, and digitization such as detector output are simulated. After experts calibrate and reconstruct the data, we extract the events, tracks, and particles we are interested in, and then physical quantities are calculated.

3.1 Event selection

Events in good condition are skimmed. The requirements are :

IsTriggerTVX – This is a condition of FT0 vertex at trigger level. Checking whether the time difference between FT0C and FT0A is acceptable. This corresponds to the minimum-bias trigger in Run 2 of the trigger measurement. Return true when the event is good.

NoTimeFrameBorder – The aim of this cut is to reject collisions close to time frame borders due to incomplete TPC drift volume. Data depletion was observed near the time frame border, and this occurred from values very close to the TPC drift time (Figure:3.1). To avoid such regions, bunch crossings are checked to determine whether they are far from the time frame borders. Return true when the event is good.

NoITSROFrameBorder – The aim of this cut is to reject events affected by the ITS Readout frame border. The reason is similar to that of Time Frame above. Return true when the event is good.

z vertex ($-10 < z_{\mathrm{vtx}} < 10$**)** – It requires that collision points be near the center of detectors.

As an example, the distribution of vertex Z before and after event selection is shown in Figure 3.2.

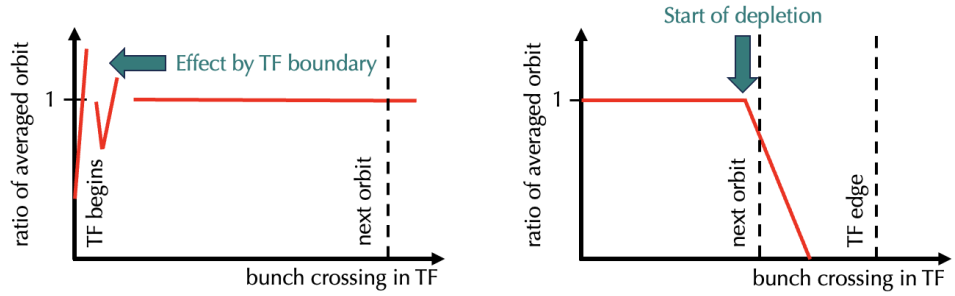

FIGURE 3.1: Illustration of the orbit ratio near the time frame border. The vertical axis represents the ratio of orbit to "average" orbit, and the horizontal axis represents the bunch crossing in time frame. At the beginning of a time frame (left), orbital information that should have been recorded in the previous time frame is intruded. Orbital depletion is observed before the the time frame edge (right).

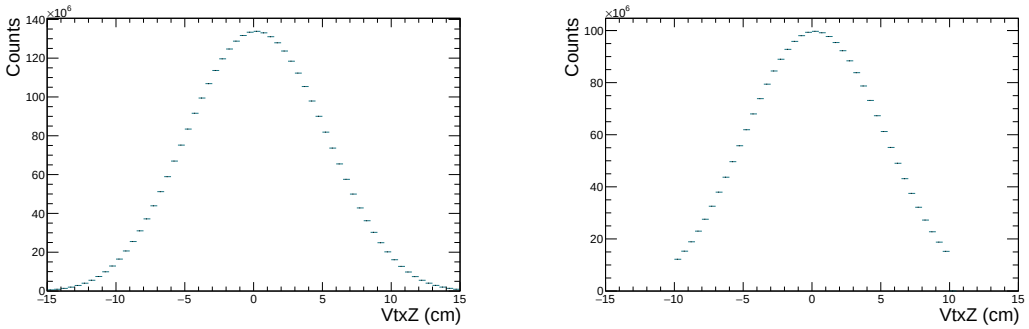

FIGURE 3.2: Vertex Z distribution before (left) and after (right) event selection in proton-proton collisions. Real data.

3.2 Track selection

Here, the particle track detected by the central barrel detectors is called “Track”. First, we need to check whether reconstructed tracks are reliable. Tracks are mainly reconstructed in the geometrical acceptance of the central detectors, especially ITS and TPC, so track quality depends on their information. The coverage of the central barrel region is $|\eta| < 0.9$. In the analysis, we usually use 0.8 instead to avoid an acceptance drop at the barrel’s border. The tracks that we want are generated from collisions, so to extract them hit information of most inner barrel layers of ITS, *i.e.*, closest to the collision point, is required. The charged particle passing through the TPC induces a signal on a pad-row. A “Cluster” is defined as those whose charge exceeds a threshold and meets all the required quality criteria. The more clusters there are, the more reliable the reconstructed track will be. A sufficient number of clusters is required to select electrons and guarantee the track quality. The sum of the squared differences between the tracks and the clusters used in the reconstruction is χ^2. The condition for good tracks is set as $\chi^2 < 4$. Table 3.1 is the list of cuts applied in this analysis.

Variable	Requirement
Pseudorapidity	$\|\eta\| < 0.8$ or 0.9
Hit on ITS IB layer	at least one hit
Number of TPC clusters	> 70
χ^2 per cluster in first iteration	< 4

TABLE 3.1: Track selection

3.3 Electron selection

The central barrel detectors detect stable charged particles (*e.g.* e, pi, K, p). We perform particle identification (PID) using the $n\sigma$-cut method with the TPC and TOF (example: Figure 3.3). The formula for TPC $n\sigma$ is:

$$n_{\sigma}^{\mathrm{TPC}} = \frac{dE/dx_{\mathrm{measured}} - dE/dx_{\mathrm{expected}}}{\sigma_{\mathrm{PID(TPC)}}} \tag{3.1}$$

where $dE/dx_{\mathrm{measured}}$is the measured energy loss in the TPC gas, $dE/dx_{\mathrm{expected}}$ is the expected energy loss for particular particle hypothesis, and $\sigma_{\mathrm{PID(TPC)}}$ is the TPC dE/dx resolution on the measurement.

Similarly, the $n\sigma$ of the TOF is given by:

$$n_{\sigma}^{\mathrm{TOF}} = \frac{t_{\mathrm{measured}} - t_{\mathrm{expected}}}{\sigma_{\mathrm{PID(TOF)}}}, \quad t_{\mathrm{measured}} = t_{\mathrm{hit}} - \mathrm{start}_{\mathrm{time}} \tag{3.2}$$

where t_{hit} is the particle arrival time measured in the TOF, $\mathrm{start}_{\mathrm{time}}$ is the event collisions time given by the FIT detector, t_{expected} is the predicted time computed by the ALICE reconstruction, which takes into account track length, momentum, and energy loss in the material, and $\sigma_{\mathrm{PID(TOF)}}$ is the resolution that depends on the TOF resolution, tracking capabilities, and the precision of the collision time of the events (Eq.(3.3)).

$$\sigma_{\mathrm{PID(TOF)}} = \sqrt{\sigma_{\mathrm{TOF}}^2 + \sigma_{\mathrm{starttime}}^2 + \sigma_{\mathrm{tracking}}^2} \tag{3.3}$$

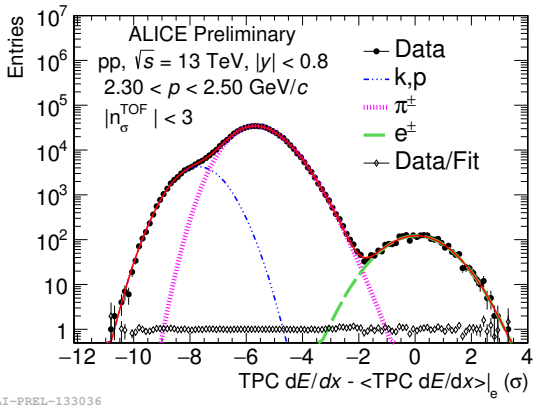

FIGURE 3.3: Simultaneous fit of the TPC nsigma signal for 2.3 GeV/c < p_T < 2.5 GeV/c [36].

The difference between the measured and predicted values must be less than a

certain threshold. Table 3.2 shows the applied cuts list. Some analyses do not use the TOF cut. The range of $n\sigma_e^{\mathrm{TPC}}$ is decided to consider pion contamination.

Variable	Requirement
TPC $n\sigma$ Electron	$-2 < n\sigma_e^{\mathrm{TPC}} < 3$
TPC $n\sigma$ Pion	$n\sigma_\pi^{\mathrm{TPC}} > 3.5$
TPC $n\sigma$ Proton	$n\sigma_p^{\mathrm{TPC}} > 3.5$
TOF $n\sigma$ Electron	$-3 < n\sigma_e^{\mathrm{TOF}} < 3$

TABLE 3.2: Electron selection

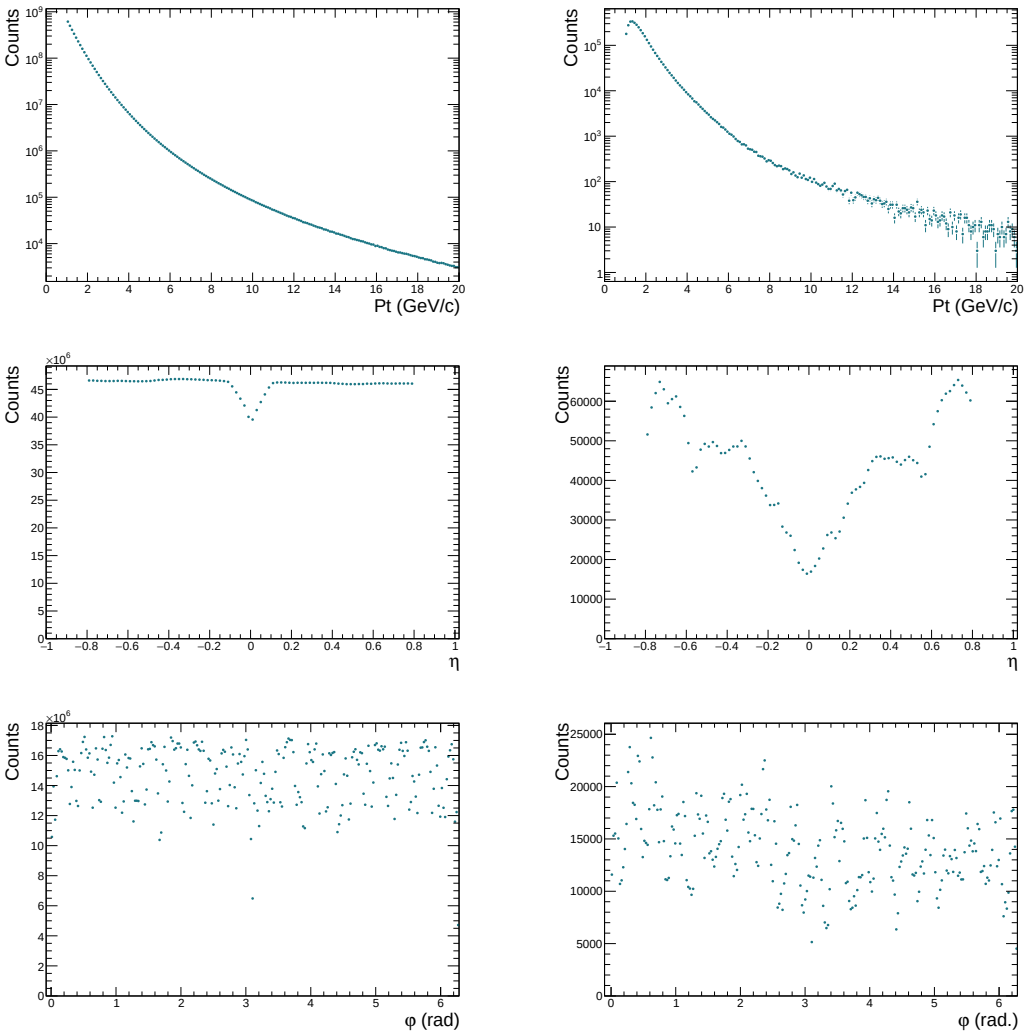

FIGURE 3.4: Distributions before (left) and after (right) electron selection in pp collisions. Real data. (Top) pT, (Middle) Eta, (Bottom) Phi.

3.4 Muon selection

The particle that penetrates the hadron absorber in front of the MCH and the iron wall in front of the MID is the muon. The requirements shown in Table 3.3 are related to this definition. The conditions of η and R_{abs} require that the particle has passed through the detector and absorber. pDCA is the product of momentum and distance closest approach (DCA), and is a condition regarding multiple scattering within the absorber. However, it is not significantly related to the selection in this case.

Variable	Requirement
Pseudorapidity	$-4.0 < \eta < -2.5$
Radius of the Absorber	$17.6 < R_{\text{abs}} < 89.5$
pDCA ($R_{\text{abs}} < 26.5$)	$0.0 < p\text{DCA} < 594.0$
pDCA ($R_{\text{abs}} > 26.5$)	$0.0 < p\text{DCA} < 324.0$
matching MCH-MID	Required
Track Type	Muon standalone

TABLE 3.3: Muon selection

The last two conditions are the selection of the detector type and track type to use. There are five types of tracks. We use the "MUON standalone Track" (blue line in Figure 3.5), which utilizes information from the MCH and MID detectors.

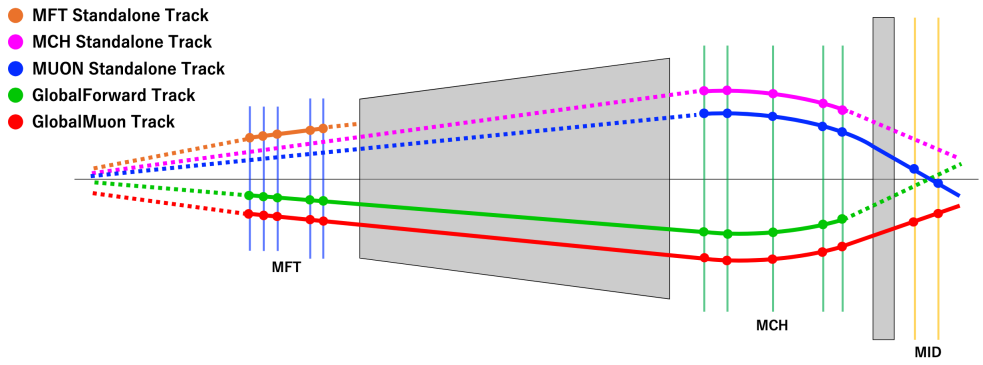

FIGURE 3.5: Definition of muon track types [37]

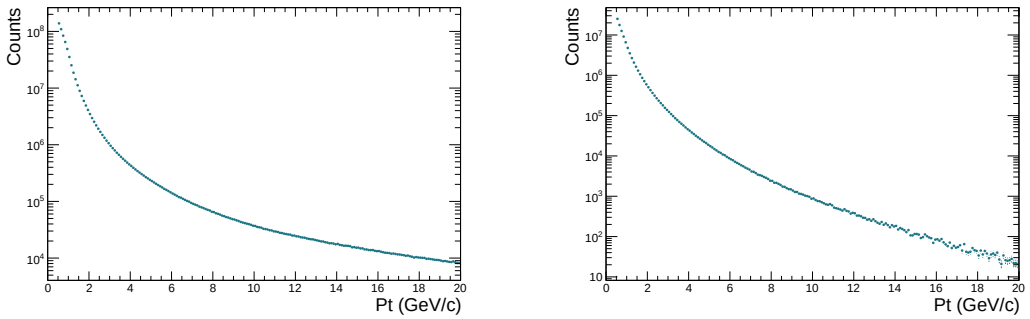

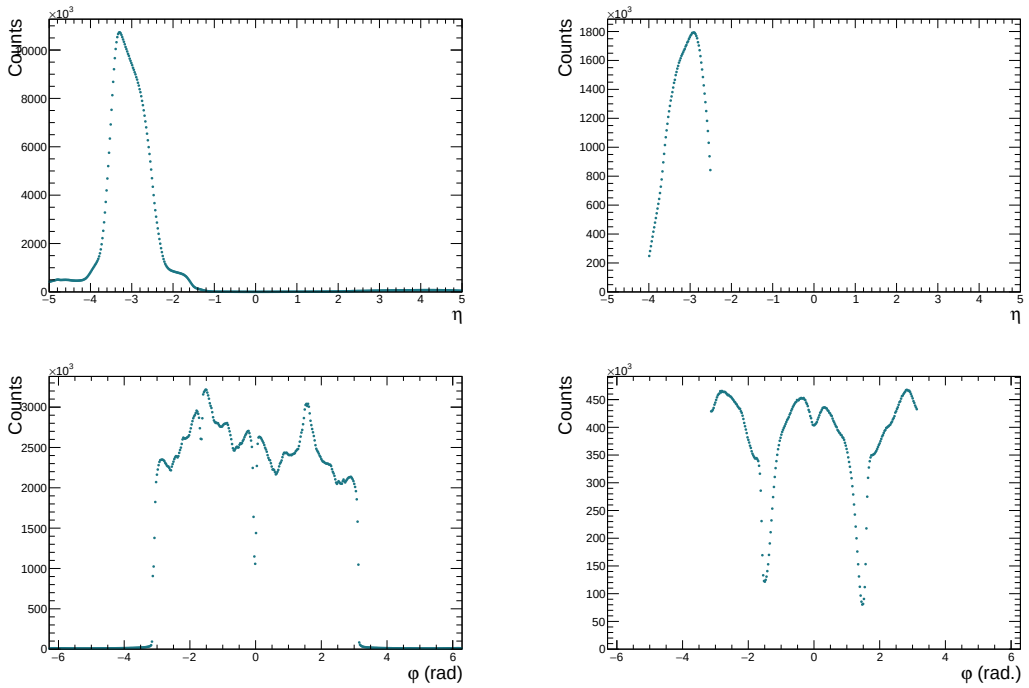

FIGURE 3.6: Distributions before (left) and after (right) muon selection in pp collisions. Real data. (Top) pT, (Middle) Eta, (Bottom) Phi.

3.5 Mass reconstruction

Mass reconstruction is one of the ways to identify unstable particles. When a particle X undergoes a two-body decay ($X \rightarrow A + B$), the invariant mass M of X is given by Eq.(3.4), using the four-momenta of particles A and B as $(E_1, \boldsymbol{p}_1)$ and $(E_2, \boldsymbol{p}_2)$, respectively:

$$M = \sqrt{(E_1 + E_2)^2 - (\boldsymbol{p}_1 \boldsymbol{p}_2)^2} \tag{3.4}$$

In an actual analysis, all possible combinations of particles within one event are calculated. Consequently, the output distribution encompasses correlated events, *e.g.*, signal and correlated backgrounds, and uncorrelated events, *i.e.*, a part of combinatorial backgrounds. This applies to all calculated pair quantities, not just mass. Figure 3.7 shows the schematic of the mass reconstruction.

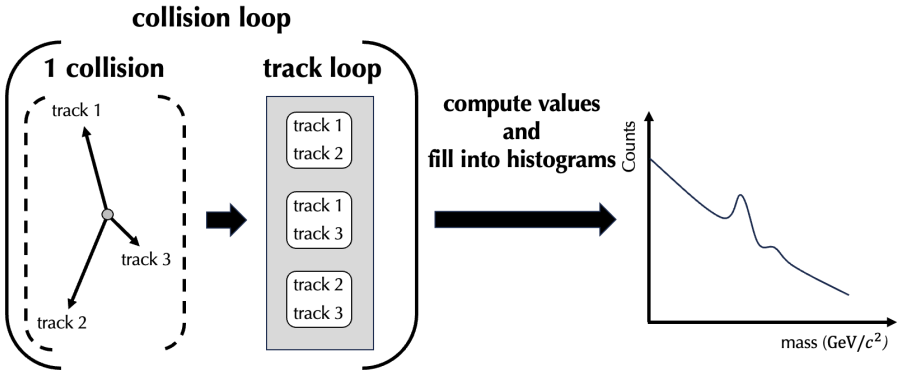

FIGURE 3.7: Schematic of the mass reconstruction

Figure 3.8 is an example of the invariant mass distribution reconstructed via electron pairs. The left figure is the one reconstructed from the opposite-sign pair (e^+e^-), and the right is one reconstructed from the like-sign pair (e^+e^+, e^-e^-). It can be seen that by performing mass reconstruction, the J/ψ peak (around 3 GeV), which is an unstable particle, can be confirmed in the left one. There is no decay of J/ψ into a like-sign pair due to the charge conservation, so no peak is seen in the right one.

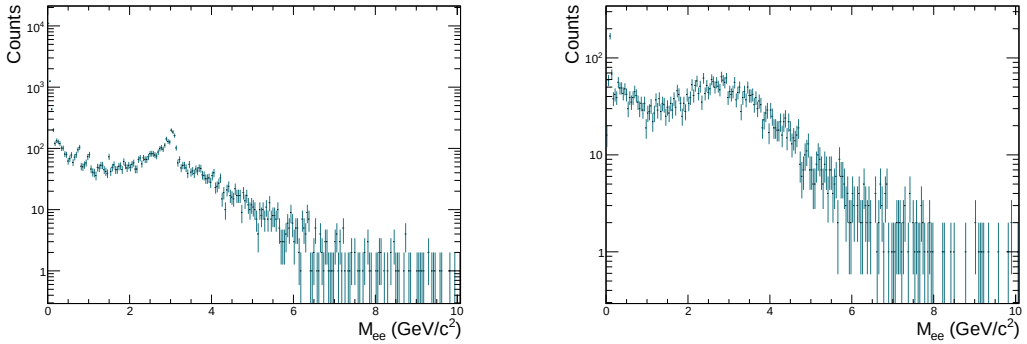

FIGURE 3.8: Invariant mass distribution reconstructed via electron pairs, opposite-sign pairs (left) and like-sign pairs (right). Real data.

3.6 Azimuthal angle distribution

The difference in the azimuthal angle between electron and muon is calculated by:

$$\Delta\varphi = \varphi_{\text{electron}} - \varphi_{\text{muon}} \tag{3.5}$$

The range of this delta phi is from -2π to 2π, whereas what we want to know is the opening angle. Therefore, an operation to fold delta phi into the range of 2π is added. By convention, it is folded to the range $-\pi/2$ to $3\pi/2$. This is because the range is suitable for checking the behavior at near- and away-side regions. The $\Delta\varphi$ distribution between electrons and muons after the folding procedure above is shown in Figure 3.9.

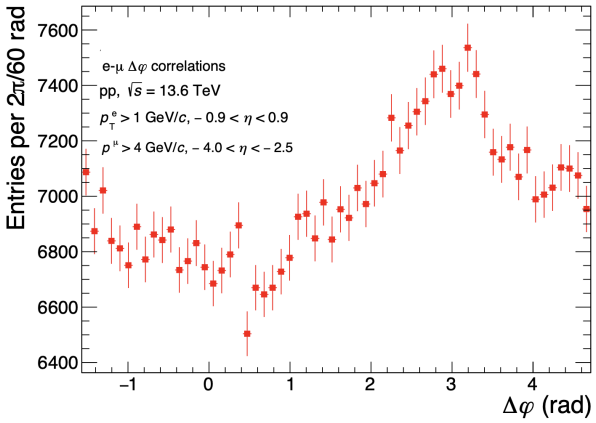

FIGURE 3.9: Azimuthal angular distribution between electrons and muons. Real data.

3.7 Heavy flavor extraction

The distribution shown in Figure 3.9 consists of pairs of inclusive electrons and muons. In correlation measurements, conditions are imposed on one of the particles to ensure that it is a heavy flavor signal. One of the simple methods is p_T cuts. Heavy-flavor hadrons have three main sources of production at LHC energies.

- Prompt charm hadrons: c $\rightarrow$ e or μ
- Non-prompt charm hadrons: b $\rightarrow$ D $\rightarrow$ e or μ
- Prompt beauty hadrons: b $\rightarrow$ e or μ

Figure 3.10 shows each source's p_T distribution of electrons. Due to the large mass, leptons from heavy-flavor hadrons dominate intermediate and high p_T regions. Therefore, the region above 2 GeV/c is extracted when good heavy-flavor correlations are desired. In addition, according to the STAR experiment [38], particles in the region above 3 GeV/c keep the direction of mother particles well.

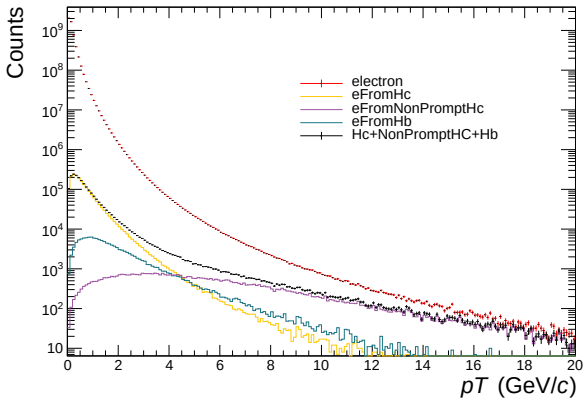

FIGURE 3.10: Electron p_T distribution for each source. MC data. Electron selection cuts have not been applied to all entries.

The p_T cut is also effective for muons. Heavy-flavor is dominant in the high p_T region. We use the region above 4 GeV/c in this analysis.

3.8 Background subtraction

The candidates of inclusive electrons and muons consist of heavy-flavor decays, non-heavy-flavor sources, and misidentified hadrons. Pairs containing particles other than those derived from heavy-flavor decays are uncorrelated, so we can remove contributions from them by estimating and subtracting the combinatorial background. There are two methods to estimate a combinatorial background.

3.8.1 Like-sign method

The like-sign method estimates the uncorrelated background in the opposite-sign pairs by the number of like-sign pairs. The yield of electron muon pairs is expressed by:

$$N^{e\mu}(\Delta\varphi) = N^{e\mu}_{HF}(\Delta\varphi) + N^{e\mu}_{HF,NHF}(\Delta\varphi) + N^{e\mu}_{NHF}(\Delta\varphi) \tag{3.6}$$

where $N^{e\mu}_{HF}(\Delta\varphi)$ is both from heavy-flavor, $N^{e\mu}_{HF,NHF}(\Delta\varphi)$ is from heavy-flavor and non-heavy-flavor or misidentified hadron, and $N^{e\mu}_{NHF}(\Delta\varphi)$ is both from non-heavy-flavor or misidentified hadron. $N^{e\mu}(\Delta\varphi)$ is decomposed into the like- and opposite-sign terms.

$$N^{e\mu}_{\text{like}}(\Delta\varphi) = N^{e\mu}_{HF,NHF,\text{like}}(\Delta\varphi) + N^{e\mu}_{NHF,\text{like}}(\Delta\varphi) \tag{3.7}$$

$$N^{e\mu}_{\text{opposite}}(\Delta\varphi) = N^{e\mu}_{HF,\text{opposite}}(\Delta\varphi) + N^{e\mu}_{HF,NHF,\text{opposite}}(\Delta\varphi) + N^{e\mu}_{NHF,\text{opposite}}(\Delta\varphi) \tag{3.8}$$

Here, since $N^{e\mu}_{HF,NHF}(\Delta\varphi)$ and $N^{e\mu}_{NHF}(\Delta\varphi)$ have no azimuthal correlation, for simplicity, we assume that the contributions to the yield are equal for the like-sign and opposite-sign:

$$N^{e\mu}_{NHF,\text{like}}(\Delta\varphi) = N^{e\mu}_{NHF,\text{opposite}}(\Delta\varphi) \tag{3.9}$$

$$N^{e\mu}_{HF,NHF,\text{like}}(\Delta\varphi) = N^{e\mu}_{HF,NHF,\text{opposite}}(\Delta\varphi) \tag{3.10}$$

Therefore, we can extract the opposite-sign signals by subtracting like-sign pairs from opposite-sign pairs.

$$N^{e\mu}_{HF}(\Delta\varphi) = N^{e\mu}_{\text{opposite}}(\Delta\varphi) - N^{e\mu}_{\text{like}}(\Delta\varphi) \tag{3.11}$$

$N^{e\mu}_{HF}(\Delta\varphi)$ consists of the signal from the charm-anti-charm pairs ($c\bar{c}$) and part of the signal from the beauty-anti-beauty pairs ($b\bar{b}$).

In a general analysis, the signal is calculated as follows, with the variable R accounting for possible charge asymmetry due to detector acceptance bias relative to charge:

$$\text{Signal} = N^{+-} - 2R\sqrt{N^{++}N^{--}} \tag{3.12}$$

$$R = \frac{N^{+-}_{ME}}{2\sqrt{N^{++}_{ME}N^{--}_{ME}}} \tag{3.13}$$

The problem with this method is that the like-sign signals derived from the $B\bar{B}$ such as decay chains and oscillations (Figure 3.11) are lost. Eq. (3.7) is precisely expressed as follows:

$$N^{e\mu}_{\text{like}}(\Delta\varphi) = N^{e\mu}_{HF,\text{like}}(\Delta\varphi) + N^{e\mu}_{HF,NHF,\text{like}}(\Delta\varphi) + N^{e\mu}_{NHF,\text{like}}(\Delta\varphi) \tag{3.14}$$

The contribution of like-sign signals corresponds to $N^{e\mu}_{HF,\text{like}}(\Delta\varphi)$. At the RHIC center-of-mass collision energies, the contribution of this term is about 1% of the final heavy-flavor electron-muon pair yield and could therefore be neglected [39]. However, plenty of beauty quarks are generated at the LHC energies, so this method is not optimal when considering beauty quarks.

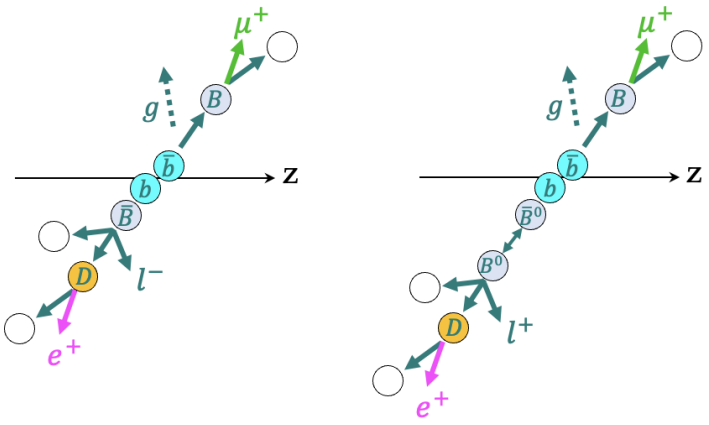

FIGURE 3.11: Example of the like-sign signal from beauty, $B \to \mu$ and $B \to D \to e$ decay chain (left) and $B^0\bar{B}^0$ oscillation (right)

3.8.2 Event-mixing method

The event-mixing method estimates the uncorrelated background using the opposite-sign pairs of two tracks collected from two different collisions from the same bin. Under certain conditions, the background shape generated by event-mixing can fully reproduce the combinatorial background. Here, satisfying these conditions means belonging to the same bin, where the same bin refers to multiplicity, Z vertex interval, and so on.

In correlation analysis, event-mixing is used to correct the geometrical acceptance effects. The correlation function between the trigger and associated particles is defined as

$$C(\Delta\eta, \Delta\varphi) = \frac{1}{N_{\text{trig}}} \frac{\mathrm{d}^2 N_{\text{assoc}}}{\mathrm{d}\Delta\eta\, \mathrm{d}\Delta\varphi} = \frac{SE(\Delta\eta, \Delta\varphi)}{ME(\Delta\eta, \Delta\varphi)} \tag{3.15}$$

where N_{trig} is the total number of trigger particles. The signal distribution $S = 1/N_{\text{trig}}\ \mathrm{d}^2 N_{\text{same}} / \mathrm{d}\Delta\eta\, \mathrm{d}\Delta\varphi$ is the associated particle's yield per trigger particles, and N_{same} is the entries of the same event. The mixed-event distribution $ME(\Delta\eta, \Delta\varphi) = \alpha\, \mathrm{d}^2 N_{\text{mixed}} / \mathrm{d}\Delta\eta\, \mathrm{d}\Delta\varphi$ reproduces the effects of geometric acceptance and uncorrelated events. α is a normalization constant that normalizes to have a value of 1 in bins where there is no pair acceptance loss or local inefficiency of the detector. If we do not do this, the number of pairs in the corrected distribution will be biased and will not reflect the actual number of pairs. For barrel-barrel correlation, at $\Delta\varphi = 0, \Delta\eta = 0$, there is no detector inefficiency or acceptance limit. Thus, we normalize the distribution by taking the criteria as $B(0,0)$ [40]. For barrel-forward correlation, there is no region with no acceptance effects. In this study, we normalize the mixed-event distribution by setting the value of the maximum acceptance region to 1 [41]. Figure 3.12 is one example of this method.

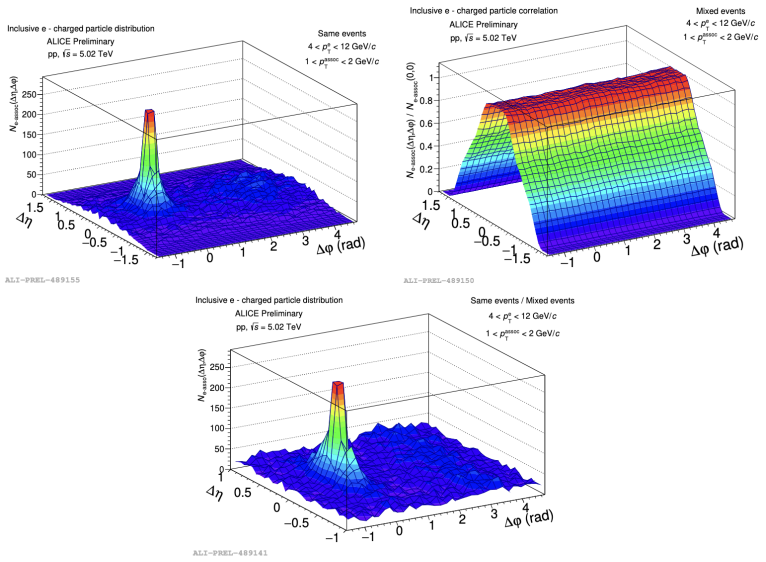

FIGURE 3.12: Procedure of the correction of geometrical acceptance effects using event-mixing methods [42].

3.9 Comparison with MC simulation

PYTHIA 8 is a high-energy particle collision event generator based on theoretical calculations and phenomenological models. In PYTHIA8, heavy flavor production consists of three processes: pair creation, flavor excitation, and gluon splitting. By comparing with real data, it is possible to constrain models and clarify the contribution of each generative process. Since there is no process that explicitly generates the NLO process, this paper only investigates the angular dependence of charm pair creation via gluon fusions for simplicity (see Table 3.4).

Setting	Condition
beam particle	proton
center-of-mass energy	13.6 TeV
process	$gg \rightarrow c\bar{c}$
tune	Monash 2013

TABLE 3.4: The settings of PYTHIA simulation

Chapter 4

Results and Discussion

4.1 Purity of single electrons and muons

This section shows the purity results using MC data. Appendix B shows the General physical quantity distributions of MC data.

4.1.1 electron

The purity of single particles is calculated by:

$$\text{Purity} = \frac{\text{Number of electrons after electron selection}}{\text{Number of particles after electron selection}} \tag{4.1}$$

The purity applying the cuts in Table 3.2 without the TOF cut is shown in Figure 4.1. The purity is below 50% and above 3 GeV/c, where the heavy flavor dominates, is about 20%.

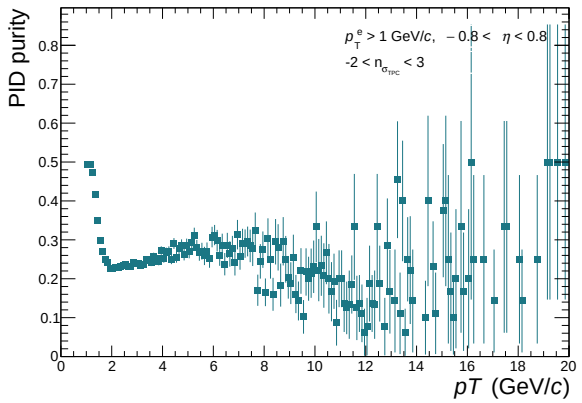

FIGURE 4.1: Purity of single electrons

The cause of low purity is hadron contamination. There are two ways to improve the purity. The first is adding the TOF cut. The aim of this cut is to remove the kaon and proton contamination. Due to the issue related to the FIT detector in MC data, we can not show the right plot after applying the TOF cut here.

The second is applying the tight TPC $n\sigma$ cut. The higher the p_T, the more pion contamination there is in the negative $n\sigma_e^{\text{TPC}}$ region, so this is reduced by applying the tight cut, $0 < n\sigma_e^{\text{TPC}} < 3$. Figure 4.2 is the results after applying the cut. The purity around $2 < p_T < 6$ GeV/c is improved, in particular, $2 < p_T < 3$ GeV/c. As can be seen from the distribution of $n\sigma$ for $2.3 < p_T < 2.5$ GeV/c shown in Figure

3.3, this is the result of vetoing the pions that were selected in $-2 < n\sigma_e^{\mathrm{TPC}} < 3$ by changing the cut to $0 < n\sigma_e^{\mathrm{TPC}} < 3$.

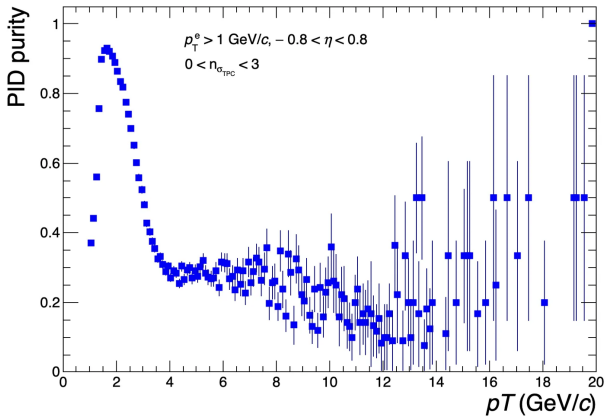

FIGURE 4.2: Purity of single electron after applying the tight TPC cut

From the above, optimizing the TPC $n\sigma$ cut each p_T interval is effective for electron identification. Essentially, in the actual analysis, we do not use MC samples for electron identification, instead identify electrons in a data-driven method that utilizes the TPC $n\sigma$ distribution for each p_T bin in the real data.

Introducing the EMCal detector is one way to improve electron identification. However, the statistics of single electrons are reduced by a factor of four. The implementation requires consideration.

4.1.2 muon

The purity applying the cuts in Table 3.3 is shown in Figure 4.3. Thanks to the hadron absorber, the purity is high. Note that there is some consideration regarding track matching between the MFT and MCH due to the multiple scattering in the hadron absorber, especially in low-momentum regions, when MFT information is used.

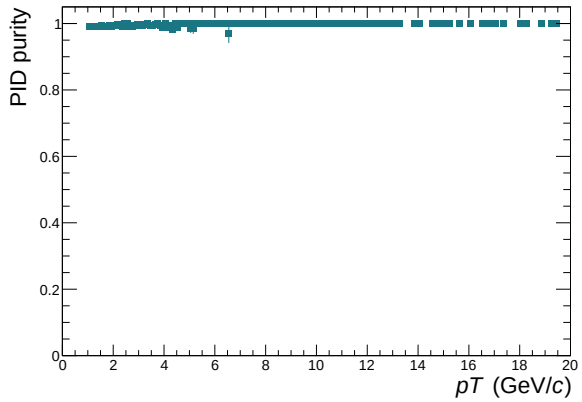

FIGURE 4.3: Purity of single muons

4.2 Pair mass, transverse momentum, and rapidity distributions

Figure 4.4 shows the distributions of physical quantity reconstructed from electron-muon pairs. The mass is calculated by Eq.(3.4). The p_T and the rapidity are the sum of two particles, *e.g.*, $p_T^{e\mu} = p_T^e + p_T^\mu$. Regarding the electron muon pairs, it is not a "real" mass distribution since we only consider one decay lepton. Thus, there is no particle peak as seen in Figure 3.8.

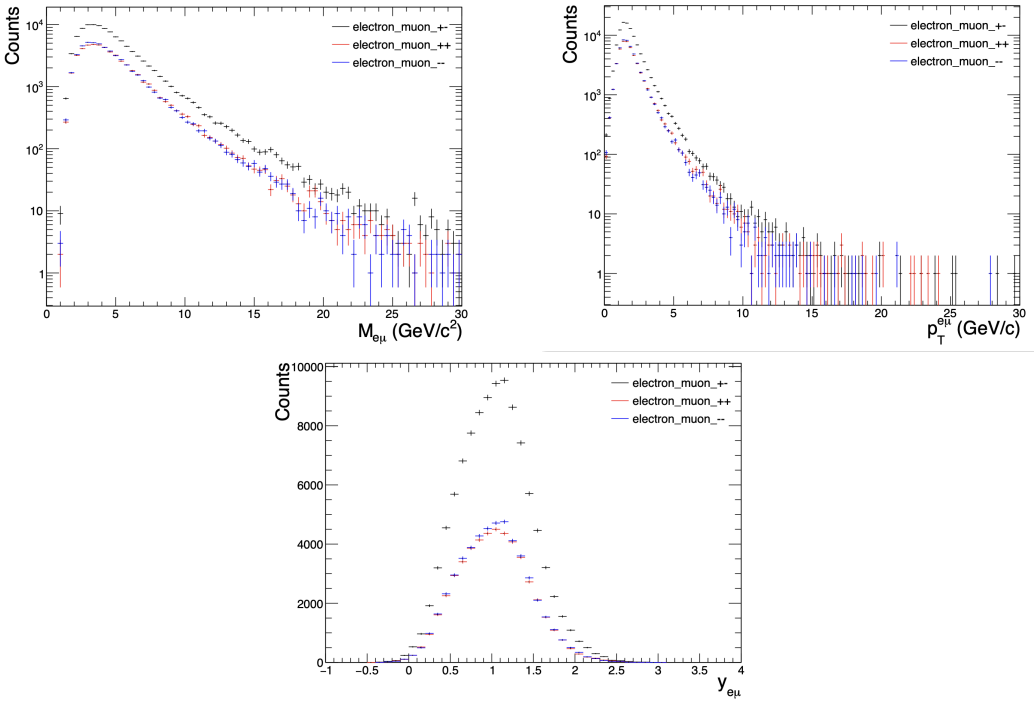

FIGURE 4.4: Distributions of electron-muon pairs. mass (upper left), pT (upper right), and rapidity (bottom).

Figure 4.5 shows the result of background subtraction using the like-sign method.

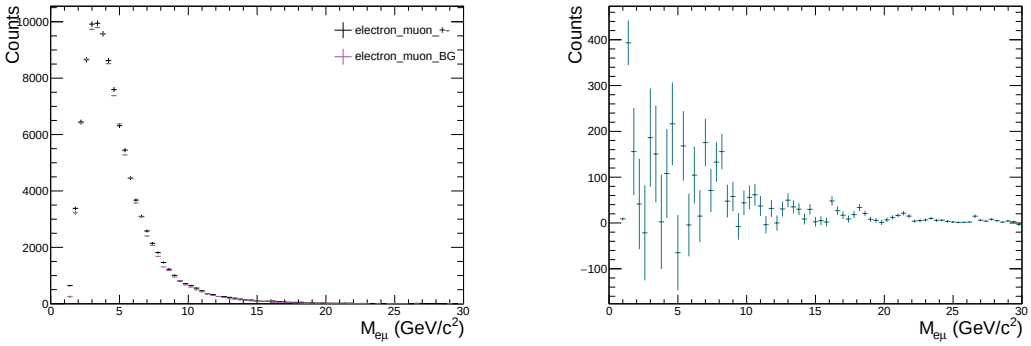

FIGURE 4.5: Background subtraction using the like-sign method. Comparison between same-event and background distributions (left), the distribution after applying background subtraction (right).

4.3 Influences depending on pT cuts

The azimuthal angular distribution between electrons and muons is shown in Figure 3.9. As mentioned in 3.7, we ensure that the particles are derived from heavy flavor by applying the p_T cuts. Figure 4.6 shows the azimuthal angular distributions after applying p_T cuts. The left histogram applies the cut regarding electrons, $p_T^e > 3\,\mathrm{GeV}/c$. The right histogram applies the cut regarding muons, $p_T^\mu > 4\,\mathrm{GeV}/c$.

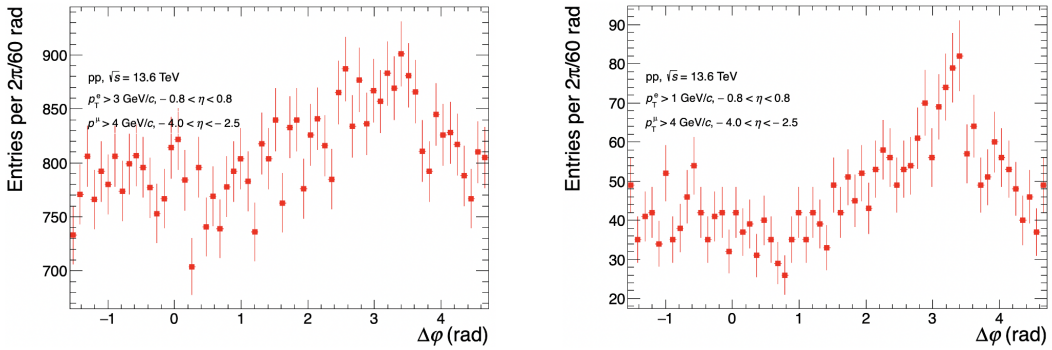

FIGURE 4.6: Azimuthal angular distribution after applying p_T cuts. 3 GeV/c cut for electrons (left), 4 GeV/c cut for muons (right).

4.4 Correction of geometrical acceptance effects

Figure 4.7 shows the $\Delta\varphi$ and $\Delta\eta$ distribution after applying the pT cuts of electrons and muons, and the distribution projected to $\Delta\varphi$. If we focus on one hand particle, *i.e.*, trigger particles, the same-event distribution is divided by the number of trigger particles (Eq. (4.2)). For instance, the number of D meson in D meson-charged particle correlation.

$$SE(\Delta\eta, \Delta\varphi) = \frac{1}{N_{\mathrm{trig}}} \frac{\mathrm{d}^2 N^{e\mu}_{\mathrm{same}}}{\mathrm{d}\Delta\eta\, \mathrm{d}\Delta\varphi} \tag{4.2}$$

Since we do not compare distributions across the different event classes, the operation dividing by N_{trig} does not perform.

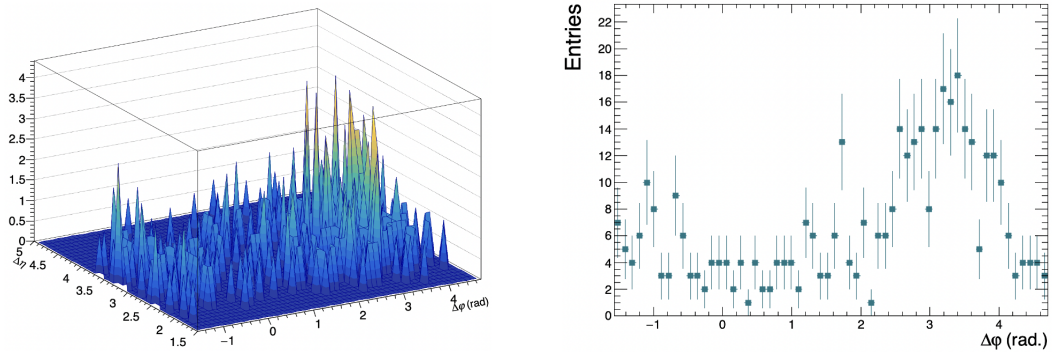

FIGURE 4.7: Distributions of same-event. $\Delta\varphi$ and $\Delta\eta$ distribution (left) and the distribution projected to $\Delta\varphi$ (right).

Figure 4.8 shows distributions of mixed-events, and distributions projecting to $\Delta\varphi$ and $\Delta\eta$ are shown in Figure 4.9. The distribution is mountain-like and spreads the range expected from the detector's rapidity coverage as a function of $\Delta\eta$, and is approximately flat as a function of $\Delta\varphi$. The fluctuation of $\Delta\varphi$ is expected due to azimuth-dependent detector inefficiencies and inhomogeneities [43]. The distribution normalized according to Eq. (4.3) is also shown in Figure 4.8 (right).

$$ME(\Delta\eta, \Delta\varphi) = \alpha \frac{\mathrm{d}^2 N^{e\mu}_{\mathrm{mixed}}}{\mathrm{d}\Delta\eta\, \mathrm{d}\Delta\varphi} \tag{4.3}$$

Here, the maximum value in the mixed-event distribution is used as normalization constant α. The specific value and its coordinates are shown in Table 4.1.

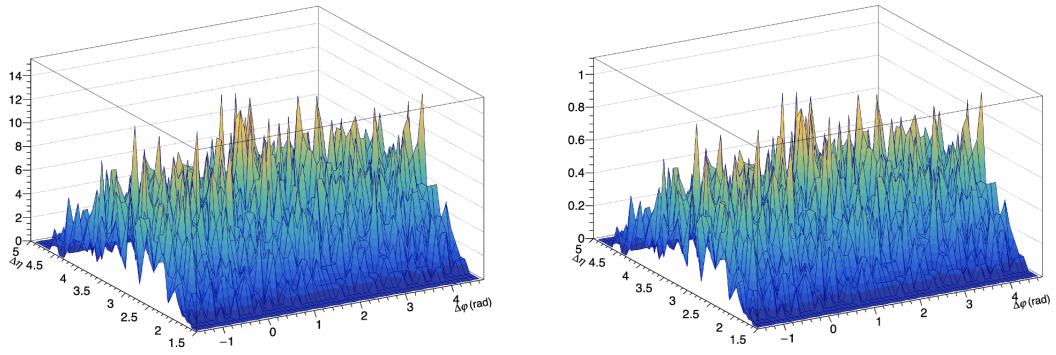

FIGURE 4.8: Distributions of mixed-event. $\Delta\varphi$ and $\Delta\eta$ distribution (left) and normalized distribution (right).

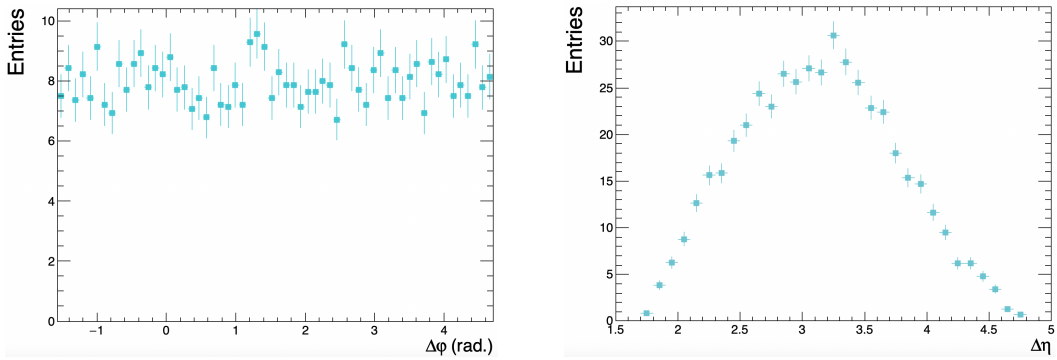

FIGURE 4.9: Projection distributions of mixed-event. $\Delta\varphi$ (left) and $\Delta\eta$ (right).

Maximum value (α)	Coordinate ($\Delta\phi, \Delta\eta$)
14	(0.994838, 3.45)

TABLE 4.1: The maximum value and its coordinates in the mixed-event distribution

The azimuthal distributions after correcting geometrical acceptance effects are shown in Figure 4.10. Although the statistics are small and the error is large, a peak can be seen around $\Delta\varphi = \pi$.

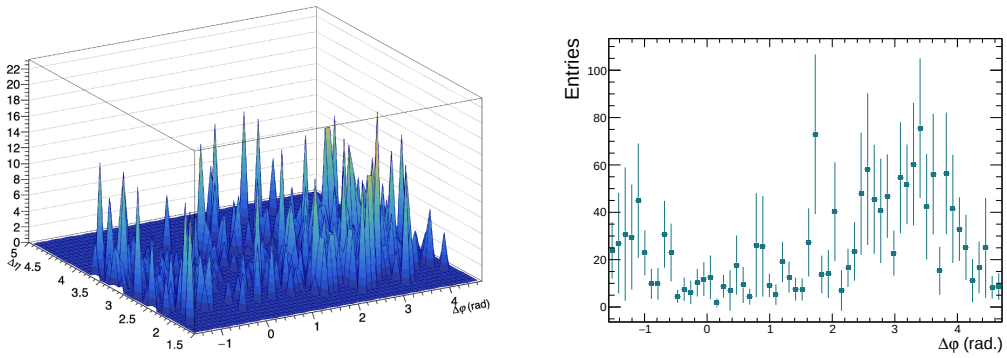

FIGURE 4.10: Distributions after applying the geometrical acceptance correction (left), and the distribution projected to $\Delta\varphi$ (right).

4.5 PYTHIA simulation study toward the comparison with real data

Figure 4.11 shows the azimuthal distribution between charm and anticharm quarks just before they decay. The number of collisions is 10^4, which means that pair production of $c\bar{c}$ has occurred 10^4 times.

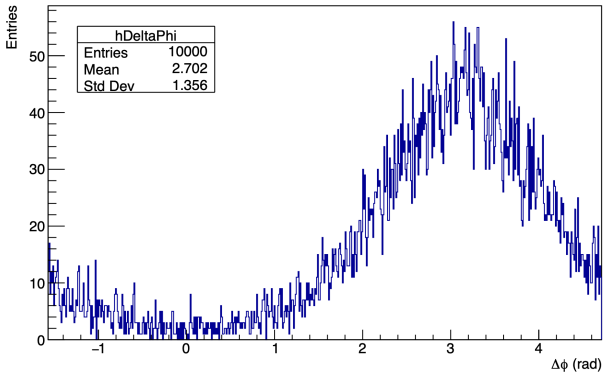

FIGURE 4.11: Azimuthal angular distribution between charm and anticharm quark. 10^4 events.

The left histogram of Figure 4.12 shows the azimuthal distribution between D mesons and anti-D mesons. Here, D mesons mean $D^{\pm}$, D^0, and D^*. Charm quarks do not necessarily hadonize to D mesons, so the number of entries is reduced. The right one is between electrons and muons from D mesons. The number of collisions for both is 10^6. Since there is no p_T cut, it also contains particles that do not retain the momentum direction of the parent particle. This is one of the reasons why the peak of the distribution is blunted.

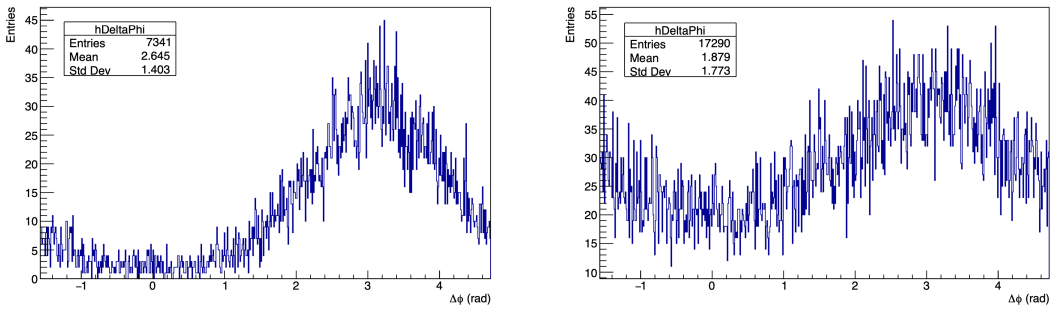

FIGURE 4.12: Azimuthal distributions, between D mesons and Anti-D mesons (left), between electrons and muons (right). 10^6 events.

The distribution of electron-muon pairs after applying the η cut is shown in Figure 4.13. The number of collisions is 10^8. It can be seen that the $\Delta\varphi = \pi$ peak, which is characteristic of the pair production signal, can also be confirmed in the electron-muon pair.

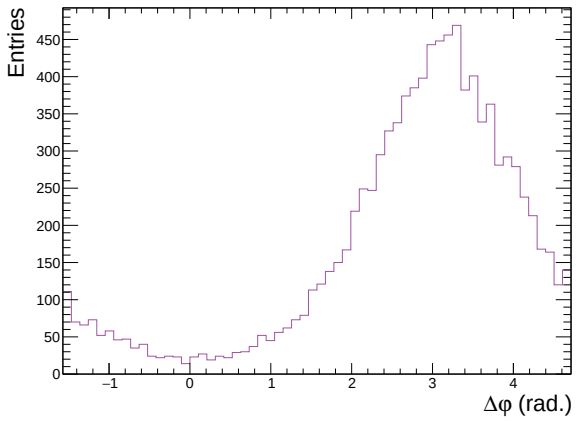

FIGURE 4.13: Azimuthal angular distribution between electrons and muons from D mesons after applying η cuts. 10^8 events.

We have not yet seen the distribution of NLO processes, nor have we properly taken into account hadronization and multiparton interactions involving non-perturbative QCD physics. In future research, we plan to take these factors into consideration.

Chapter 5

Conclusion

In this study, latest results from the first electron-muon measurement from the ALICE experiment are presented. An assessment of single-electron and single-muon purity using MC data is performed. The electron purity is about 20%, so a more appropriate cut should be used. A data-driven method is planned to evaluate and optimize the electron identification for each pT range using real data. The purity of muons looks good. The analysis including the MFT is expected. Using the above identification conditions, the azimuthal distribution between electrons and muons is obtained. p_T cuts are applied to extract the signal from the heavy flavor. The distribution after the cut is then modified using the event-mixing method to eliminate the influence of detector acceptance on the distribution. Figure 5.1 shows the azimuthal correlation between the corrected real data and $c\bar{c}$ pair generation by PYTHIA8. There are many contributions we have not taken into account, so the two do not match except for the tendency for the peak to be at $\Delta\varphi = \pi$.

By increasing the amount of statistics and comparing the azimuthal distribution for each p_T and the contribution of each process using MC data, we can approach the cross section for heavy flavor production and the center-of-mass collision energy dependence of the production mechanism. The ultimate goal is to investigate the physical properties of the QGP through measurements in heavy ion collisions. This study is a first step toward that goal.

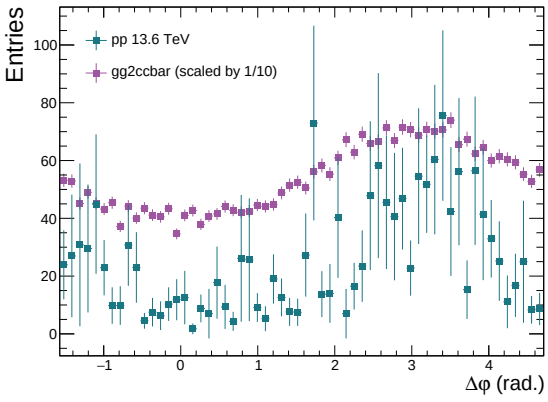

FIGURE 5.1: Azimuthal angular distributions of real data and PYTHIA8 simulation.

Appendix A

Coupling constant

A.1 QED

The correction factor $B(Q^2)$ for the coupling constant α by the vacuum polarization is [1]:

$$\alpha_0 B(Q^2) \equiv -\Pi_\gamma(q^2 = -Q^2)$$

$$\begin{cases} \fallingdotseq -\frac{\alpha_0}{3\pi}\left\{\Delta_e - \ln\left(\frac{Q^2}{m_e^2}\right)\right\} & Q^2 \gg m_e^2 \\ \fallingdotseq -\frac{\alpha_0}{3\pi}\left\{\Delta_e - \ln\left(\frac{Q^2}{5m_e^2}\right)\right\} & Q^2 \ll m_e^2 \end{cases} \tag{A.1}$$

where α_0 is a bare coupling constant, $q^2 = -Q^2 < 0$ is the square of momentum transfer of the virtual photon, and Δ_e is a part of the ultraviolet divergence. The effective charge α_{eff} is represented by the sum of all loops causing vacuum polarization.

$$\alpha_{\text{eff}} = \alpha_0\{1 + \alpha_0 B + 1 + \alpha_0 B \alpha_0 B + \cdots\} = \frac{\alpha_0}{1 - \alpha_0 B(Q^2)} \tag{A.2}$$

The value that the test charge feels at a sufficient distance $(Q^2 \to 0)$ can be regarded as the actual charge being measured α, so that if

$$\alpha \equiv \alpha_{\text{eff}}(0) = \frac{\alpha_0}{1 - \alpha_0 B(0)} = 1/137.\cdots \tag{A.3}$$

, then the effective coupling constant of QED is:

$$\frac{1}{\alpha_{\text{eff}}} = \frac{1}{\alpha} - \{B((Q^2) - B(0)\} \fallingdotseq \frac{1}{\alpha} - \frac{1}{3\pi}\ln\left(\frac{Q^2}{m_e^2}\right) \tag{A.4}$$

$$\therefore \alpha_{\text{eff}} = \frac{\alpha}{1 - \frac{\alpha}{3\pi}\ln\left(\frac{Q^2}{m_e^2}\right)} \tag{A.5}$$

Appendix B

General physical quantity distributions of MC data

B.1 Single Electron

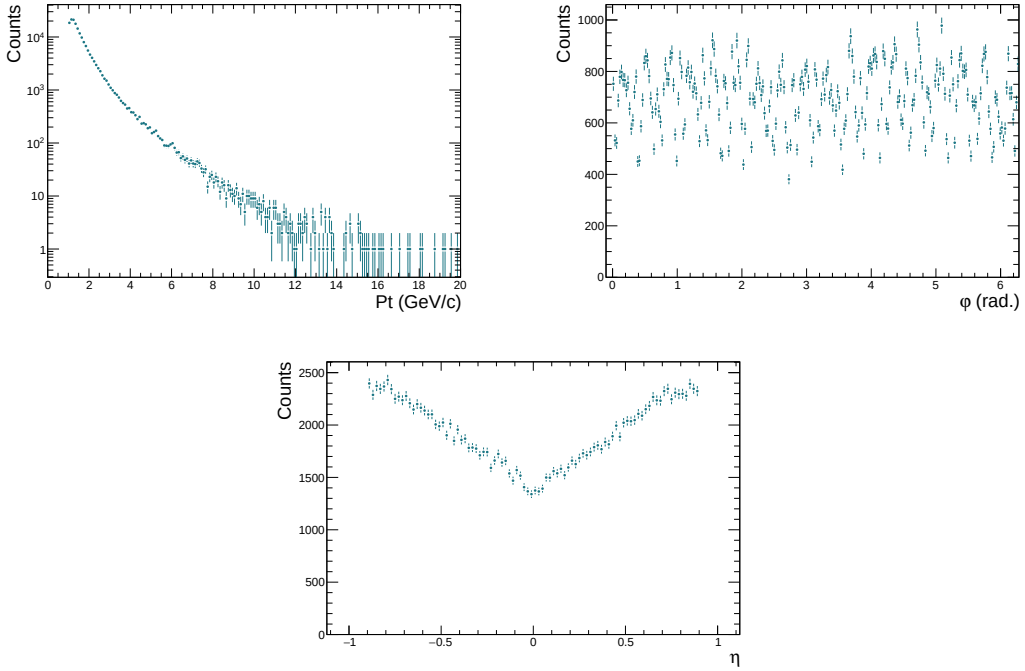

FIGURE B.1: Single electron distributions of MC data

B.2 Single Muon

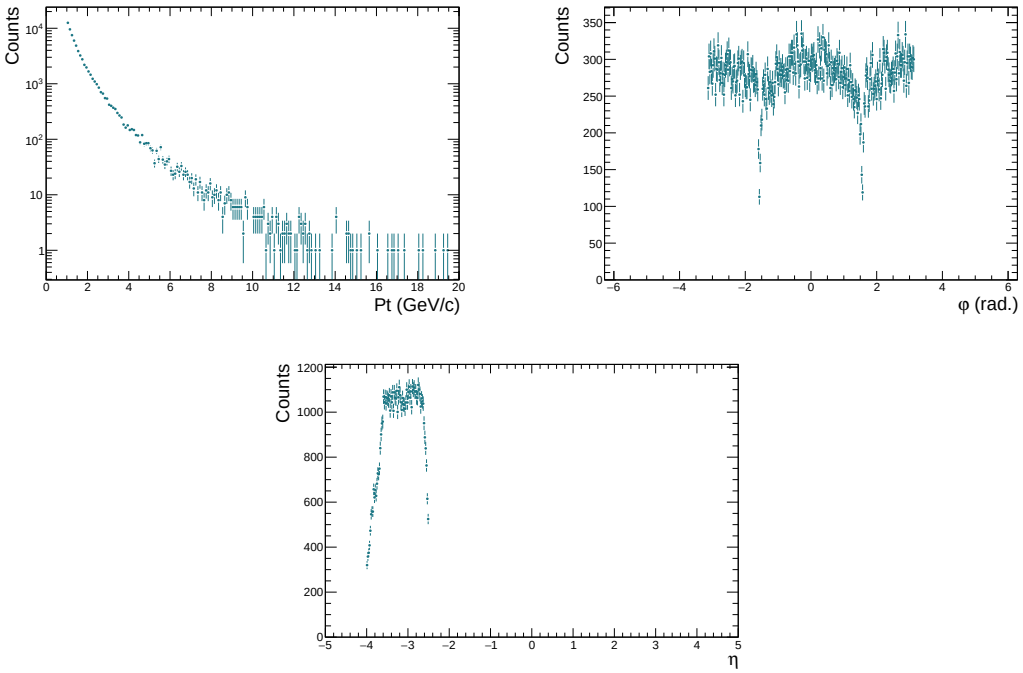

FIGURE B.2: Single muon distributions of MC data

Bibliography

[1] Yorikiyo Nagashima. *Soryuushi Hyoujun Riron to Jikkennteki Kiso*. Vol. 5. Asakurabuturigakutaikei. Asakura Shoten, 1999.

[2] Particle Data Group et al. "Review of Particle Physics". In: *Progress of Theoretical and Experimental Physics* 2022.8 (Aug. 2022), p. 083C01. ISSN: 2050-3911. DOI: 10.1093/ptep/ptac097. eprint: https://academic.oup.com/ptep/article-pdf/2022/8/083C01/49175539/ptac097.pdf. URL: https://doi.org/10.1093/ptep/ptac097.

[3] S Acharya et al. "Measurement of beauty-quark production in pp collision at $\sqrt{s}$ = 13 TeV via non-prompt D mesons". In: *J. High Energ. Phys.* 10 (2024), p. 110. DOI: 10.1007/JHEP10(2024)110.

[4] Shreyasi Acharya et al. "Charm production and fragmentation fractions at midrapidity in pp collisions at $\sqrt{s}$ = 13 TeV". In: *JHEP* 12 (2023), p. 086. DOI: 10.1007/JHEP12(2023)086. arXiv: 2308.04877 [hep-ex].

[5] S. Acharya et al. "First measurement of ■$_c^+$ production down to $p_T = 0$ in pp and p-Pb collisions at $\sqrt{s_{NN}} = 5.02$ TeV". In: *Phys. Rev. C* 107 (6 June 2023), p. 064901. DOI: 10.1103/PhysRevC.107.064901. URL: https://link.aps.org/doi/10.1103/PhysRevC.107.064901.

[6] Roel Aaij et al. "Enhanced Production of Λb0 Baryons in High-Multiplicity pp Collisions at s=13 TeV". In: *Phys. Rev. Lett.* 132.8 (2024), p. 081901. DOI: 10.1103/PhysRevLett.132.081901. arXiv: 2310.12278 [hep-ex].

[7] Aram Hayrapetyan et al. "Multiplicity dependence of charm baryon and baryon meson production in pPb collisions at $\sqrt{s_{NN}}$ = 8.16 TeV". In: (July 2024). arXiv: 2407.13615 [nucl-ex].

[8] Rabah Abdul Khalek, Jacob J. Ethier, and Juan Rojo. "Nuclear parton distributions from lepton-nucleus scattering and the impact of an electron-ion collider". In: *Eur. Phys. J. C* 79.6 (2019), p. 471. DOI: 10.1140/epjc/s10052-019-6983-1. arXiv: 1904.00018 [hep-ph].

[9] Carlota Andres, Fabio Dominguez, and Marcos Gonzalez Martinez. "From soft to hard radiation: the role of multiple scatterings in medium-induced gluon emissions". In: *JHEP* 03 (2021), p. 102. DOI: 10.1007/JHEP03(2021)102. arXiv: 2011.06522 [hep-ph].

[10] Shreyasi Acharya et al. "Measurement of beauty production via non-prompt charm hadrons in p–Pb collisions at $\sqrt{s_{NN}}$ = 5.02 TeV". In: *JHEP* 11 (2024), p. 148. DOI: 10.1007/JHEP11(2024)148. arXiv: 2407.10593 [nucl-ex].

[11] S Acharya, Adamová D, et al. "The ALICE experiment: a journey through QCD". In: *Eur. Phys. J. C* 84 (2024), p. 813. URL: https://doi.org/10.1140/epjc/s10052-024-12935-y.

[12] S. Acharya et al. "Azimuthal Anisotropy of Heavy-Flavor Decay Electrons in p-Pb Collisions at $\sqrt{s_{NN}} = 5.02$ TeV". In: *Phys. Rev. Lett.* 122 (7 Feb. 2019), p. 072301. DOI: 10.1103/PhysRevLett.122.072301. URL: https://link.aps.org/doi/10.1103/PhysRevLett.122.072301.

[13] G. Aad, B. Abbott, K. Abeling, et al. "Azimuthal Angle Correlations of Muons Produced via Heavy-Flavor Decays in 5.02 TeV Pb + Pb and pp Collisions with the ATLAS Detector". In: *Phys. Rev. Lett.* 132 (20 May 2024), p. 202301. DOI: 10.1103/PhysRevLett.132.202301. URL: https://link.aps.org/doi/10.1103/PhysRevLett.132.202301.

[14] R. D. Field. "Sources of b quarks at the Fermilab Tevatron and their correlations". In: *Phys. Rev. D* 65 (9 Apr. 2002), p. 094006. DOI: 10.1103/PhysRevD.65.094006. URL: https://link.aps.org/doi/10.1103/PhysRevD.65.094006.

[15] T Åkesson et al. "A study of electron-muon pair production in 450 GeV/c pBe collisions". In: *Z. Phys. C* 72 (1996), pp. 429–436. DOI: 10.1007/s002880050262. URL: https://cds.cern.ch/record/297791.

[16] A. Adare et al. "Heavy-flavor electron-muon correlations in $p + p$ and $d + \mathrm{Au}$ collisions at $\sqrt{s_{NN}} = 200$ GeV". In: *Phys. Rev. C* 89 (3 Mar. 2014), p. 034915. DOI: 10.1103/PhysRevC.89.034915. URL: https://link.aps.org/doi/10.1103/PhysRevC.89.034915.

[17] Fabienne Landua. *The CERN accelerator complex layout in 2022. Complexe des accélérateurs du CERN en janvier 2022*. General Photo. 2022. URL: https://cds.cern.ch/record/2813716.

[18] ATLAS JAPAN. *Superconducting magnets of the LHC*. 2008. URL: https://atlas.kek.jp/old/sub/poster/SCmagnet-poster/SCmagnetPosterV1J.pdf.

[19] A. Ferretti. *The ALICE Experiment Upgrades*. Jan. 2022. DOI: 10.48550/arXiv.2201.08871.

[20] Raphael Tieulent. *ALICE Upgrades: Plans and Potentials*. 2015. arXiv: 1512.02253 [nucl-ex]. URL: https://arxiv.org/abs/1512.02253.

[21] ALICE TPC collaboration, J. Adolfsson, M. Ahmed, et al. "The upgrade of the ALICE TPC with GEMs and continuous readout". In: *Journal of Instrumentation* 16.03 (Mar. 2021), P03022. DOI: 10.1088/1748-0221/16/03/P03022. URL: https://dx.doi.org/10.1088/1748-0221/16/03/P03022.

[22] Xiaozhi Bai. *The upgraded TPC for ALICE in LHC Run 3*. 2023. URL: https://indico.ihep.ac.cn/event/19316/contributions/143566/attachments/72757/88685/cepc_nanjing_xbai_v2.pdf.

[23] Erik Brücken and Timo Hildén. "GEM Foil Quality Assurance For The ALICE TPC Upgrade". In: *EPJ Web of Conferences* 174 (2018). Ed. by S. Dalla Torre et al., p. 03004. ISSN: 2100-014X. DOI: 10.1051/epjconf/201817403004. URL: http://dx.doi.org/10.1051/epjconf/201817403004.

[24] *Gas Electron Multipliers (GEMs)*. URL: https://flc.desy.de/tpc/basics/gem/index_eng.html (visited on 01/13/2025).

[25] J. Adam et al. "Determination of the event collision time with the ALICE detector at the LHC". In: *The European Physical Journal Plus* 132 (Feb. 2017). DOI: 10.1140/epjp/i2017-11279-1.

[26] *TOF Beta vs Momentum performance in Pb-Pb at 5.02 TeV (LHC15o)*. URL: https://alice-figure.web.cern.ch/node/9150 (visited on 01/14/2025).

[27] S. Acharya et al. "Performance of the ALICE Electromagnetic Calorimeter". In: *Journal of Instrumentation* 18.08 (Aug. 2023), P08007. DOI: 10.1088/1748-0221/18/08/P08007. URL: https://dx.doi.org/10.1088/1748-0221/18/08/P08007.

[28] A. Badalà et al. "Characterization of avalanche photodiodes (APDs) for the electromagnetic calorimeter in the ALICE experiment". In: *Nuclear Instruments and Methods in Physics Research Section A: Accelerators, Spectrometers, Detectors and Associated Equipment* 596.1 (2008). Proceedings of the 8th International Conference on Large Scale Applications and Radiation Hardness of Semiconductor Detectors, pp. 122–125. ISSN: 0168-9002. DOI: https://doi.org/10.1016/j.nima.2008.07.133. URL: https://www.sciencedirect.com/science/article/pii/S0168900208010620.

[29] ALICE Collaboration. *Measurement of electrons from heavy-flavour hadron decays as a function of multiplicity in p-Pb collisions at $\sqrt{s_{\mathrm{NN}}}$ = 5.02 TeV*. Oct. 2019. DOI: 10.48550/arXiv.1910.14399.

[30] Alla Maevskaya. *ALICE FIT data processing and performance during LHC Run 3*. 2020. arXiv: 2012.02760 [physics.ins-det]. URL: https://arxiv.org/abs/2012.02760.

[31] Maciej Slupecki. "Fast Interaction Trigger for ALICE upgrade". In: *Nuclear Instruments and Methods in Physics Research Section A: Accelerators, Spectrometers, Detectors and Associated Equipment* 1039 (2022), p. 167021. ISSN: 0168-9002. DOI: https://doi.org/10.1016/j.nima.2022.167021. URL: https://www.sciencedirect.com/science/article/pii/S0168900222004466.

[32] MFT Collaboration ALICE. *ALICE Muon Forward Tracker (MFT)*. General Photo. 2020. URL: https://cds.cern.ch/record/2748310.

[33] *Addendum of the Letter of Intent for the upgrade of the ALICE experiment : The Muon Forward Tracker*. Tech. rep. Final submission of the presetn LoI addendum is scheduled for September 7th. Geneva: CERN, 2013. URL: https://cds.cern.ch/record/1592659.

[34] *Muon Spectrometer*. URL: https://alice-collaboration.web.cern.ch/menu_proj_items/Muon-Spect (visited on 01/17/2025).

[35] P Buncic, M Krzewicki, and P Vande Vyvre. *Technical Design Report for the Upgrade of the Online-Offline Computing System*. Tech. rep. 2015. URL: https://cds.cern.ch/record/2011297.

[36] Camila De Conti. *Fit of the TPC Nsigma*. 2017. URL: https://alice-figure.web.cern.ch/node/11708.

[37] Koki Soeda. *Feasibility evaluation of heavy flavor particle identification based on hadron decay point reconstruction with ALICE Muon Forward Tracker*. 2024. URL: https://www.quark.hiroshima-u.ac.jp/thesis/m202403_soeda.pdf.

[38] Gang Wang. "Non-photonic electron-hadron correlations at STAR". In: *J. Phys. G* 35 (2008). Ed. by Jan-e Alam et al., p. 104107. DOI: 10.1088/0954-3899/35/10/104107. arXiv: 0804.4448 [nucl-ex].

[39] A. Adare et al. "Heavy-flavor electron-muon correlations in $p+p$ and $d+$Au collisions at $\sqrt{s_{NN}} = 200$ GeV". In: *Phys. Rev. C* 89 (3 Mar. 2014), p. 034915. DOI: 10.1103/PhysRevC.89.034915. URL: https://link.aps.org/doi/10.1103/PhysRevC.89.034915.

[40] Shreyasi Acharya et al. *J/ψ-hadron correlations at midrapidity in pp collisions at $\sqrt{s}$ = 13 TeV*. Sept. 2024. arXiv: 2409.04364 [nucl-ex].

[41] J. Adam, D. Adamová, M.M. Aggarwal, et al. "Forward-central two-particle correlations in p–Pb collisions at sNN=5.02 TeV". In: *Physics Letters B* 753 (2016), pp. 126–139. ISSN: 0370-2693. DOI: https://doi.org/10.1016/j.physletb.2015.12.010. URL: https://www.sciencedirect.com/science/article/pii/S0370269315009533.

[42] Ravindra Singh. "Angular correlations of heavy-flavour hadron decay electrons and charged particles in pp collisions at $\sqrt{s}$ = 5.02 TeV with ALICE at the LHC". In: *PoS* LHCP2021 (2021), p. 191. DOI: 10.22323/1.397.0191.

[43] Betty Bezverkhny Abelev et al. "Long-range angular correlations of ß, K and p in p-Pb collisions at $\sqrt{s_{NN}}$ = 5.02 TeV". In: *Phys. Lett. B* 726 (2013), pp. 164–177. DOI: 10.1016/j.physletb.2013.08.024. arXiv: 1307.3237 [nucl-ex].